

# A 500 pc volume-limited sample of hot subluminoous stars

## I. Space density, scale height, and population properties

H. Dawson<sup>1</sup>, S. Geier<sup>1</sup>, U. Heber<sup>2</sup>, I. Pelisoli<sup>3,1</sup>, M. Dorsch<sup>1,2</sup>, V. Schaffenroth<sup>4,1</sup>, N. Reindl<sup>5,1</sup>, R. Culpan<sup>1</sup>, M. Pritzkuileit<sup>1</sup>, J. Vos<sup>8,1</sup>, A. A. Soemiro<sup>1,15</sup>, M. M. Roth<sup>1,15</sup>, D. Schneider<sup>2</sup>, M. Uzundag<sup>19,6,7</sup>, M. Vučković<sup>6</sup>, L. Antunes Amaral<sup>6,7</sup>, A. G. Istrate<sup>9</sup>, S. Justham<sup>10,24</sup>, R. H. Østensen<sup>11</sup>, Telting, J. H.<sup>12,21</sup>, A. A. Djupvik<sup>12,21</sup>, R. Raddi<sup>13</sup>, E. M. Green<sup>14</sup>, C. S. Jeffery<sup>16</sup>, S. O. Kepler<sup>17</sup>, J. Munday<sup>3,20</sup>, T. Steinmetz<sup>20,22,23</sup>, and T. Kupfer<sup>25</sup>

(Affiliations can be found after the references)

Received ; Accepted February 21, 2024

### ABSTRACT

We present the first volume-limited sample of spectroscopically confirmed hot subluminoous stars out to 500 pc, defined using the accurate parallax measurements from the *Gaia* space mission data release 3 (DR3). The sample comprises a total of 397 members, with 305 (~ 77%) identified as hot subdwarf stars, including 83 newly discovered systems. Of these, we observe that 178 (~ 58%) are hydrogen-rich sdBs, 65 are sdOBs (~ 21%), 32 are sdOs (~ 11%), and 30 are He-sdO/Bs (~ 10%). Among them, 48 (~ 16%) exhibit an infrared excess in their spectral energy distribution fits, suggesting a composite binary system. The hot subdwarf population is estimated to be 90% complete, assuming that most missing systems are these composite binaries located within the main sequence (MS) in the *Gaia* colour-magnitude diagram (CMD). The remaining sources in the sample include cataclysmic variables (CVs), blue horizontal branch stars (BHBs), hot white dwarfs (WDs), and MS stars. We derived the mid-plane density  $\rho_0$  and scale height  $h_z$  for the non-composite hot subdwarf star population using a hyperbolic sechant profile (sech<sup>2</sup>). The best-fit values are  $\rho_0 = 5.17 \pm 0.33 \times 10^{-7}$  stars/pc<sup>3</sup> and  $h_z = 281 \pm 62$  pc. When accounting for the composite-colour hot subdwarfs and their estimated completeness, the mid-plane density increases to  $\rho_0 = 6.15^{+1.16}_{-0.53} \times 10^{-7}$  stars/pc<sup>3</sup>. This corrected space density is an order of magnitude lower than predicted by population synthesis studies, supporting previous observational estimates.

**Key words.** stars: subdwarfs – catalogs – stars: binaries – stars: Hertzsprung–Russell and colour-magnitude diagrams – stars: statistics

### 1. Introduction

Since their serendipitous discovery by Humason & Zwicky (1947) as faint blue stars at high galactic latitudes, hot subluminoous stars have been characterised by their position in the Hertzsprung–Russell Diagram (HRD) as having lower intrinsic luminosities compared to early-type main sequence (MS) stars of similar colour. This region of the HRD between the MS and the white dwarfs (WDs) hosts many types of stars, each with its own associated evolutionary path. The hot subdwarf stars of spectral type B and O (sdBs and sdOs) compose a prominent subgroup of this population. They have since been associated with, although not restricted to, the extreme horizontal branch (EHB, Greenstein & Sargent 1974; Newell & Sadler 1978; Heber et al. 1984) and the helium main sequence (Paczynski 1971), or have evolved beyond these stages to even higher temperatures. However, to qualify for the EHB in the canonical sense, the progenitor must be stripped of nearly its entire hydrogen envelope during core He burning. Since the majority of hot subdwarfs have masses close to the core-helium-flash mass of  $\approx 0.47 M_\odot$  (Fontaine et al. 2012; Schaffenroth et al. 2022), stripping is often associated with the tip of the red giant branch (RGB) for low-mass stars with degenerate cores (Dorman & Rood 1993). However, since an intermediate mass (2.3 – 8  $M_\odot$ ) possible red giant progenitor may ignite helium in its non-degenerate core at an earlier stage, hot subdwarf stars are not restricted to this specific final mass (Han et al. 2002; Hu et al. 2008; Prada Moroni & Straniero 2009; Götberg et al. 2018). Regardless, the result is a hotter and more compact object than canonical horizontal branch (HB) stars with surface gravity and

effective temperature ranges of  $T_{\text{eff}} = 20\,000 - 40\,000$  K and  $\log g = 4.5 - 6.2$  dex, and with radii between  $0.15 R_\odot$  and  $0.35 R_\odot$  (see Heber 2016, for a complete review). Consequently, they will not ascend the asymptotic giant branch (AGB), but instead will evolve directly towards the WD cooling track.

The large amount of mass loss required to form EHB stars at the point of He burning is difficult to explain in the context of single-star evolution, and remains a missing piece of the puzzle in stellar evolution theory. Although single-star scenarios are still discussed (Sweigart 1997; Castellani & Castellani 1993; Miller Bertolami et al. 2008), decades of observational research have revealed a high binary fraction in these stars, which either host compact companions like WDs or low-mass MS stars in close binaries (Maxted et al. 2001; Napiwotzki et al. 2004; Geier et al. 2022; Schaffenroth et al. 2022, 2023) or cool MS stars in wide binaries (Stark & Wade 2003; Barlow et al. 2012, 2013; Vos et al. 2012, 2013), or otherwise have provided strong evidence of binary interaction (Pelisoli et al. 2020). This shifted the focus to binary evolution scenarios invoking three main formation channels regarding common-envelope evolution (CEE, Paczynski 1976), Roche-lobe overflow (RLOF, Han et al. 2002; Chen et al. 2013), and mergers (e.g. He-WD + He-WD mergers (Webbink 1984), CEE mergers (Politano et al. 2008), hybrid mergers (Justham et al. 2011), and He-WD + low-mass MS mergers (Clausen & Wade 2011)), the last of these may explain the observed population of single hot subdwarf stars (e.g. Napiwotzki et al. 2004; Geier et al. 2022). This motivated Han et al. (2002, 2003), and later Clausen et al. (2012), to perform a detailed binary population synthesis (BPS) study of the formation of EHB stars. The

primary objective of these studies was to discern the relative importance of the three main evolutionary channels leading to their formation, and how different combinations of input parameters can alter the resulting population properties. A key statistical parameter derived in Han et al. (2002, 2003) is the space number density,  $\rho$ , which was found to be  $\rho = 1 \times 10^{-5}$  stars/pc<sup>3</sup> and corresponds to a total of 2.4–9.5 million hot subdwarf stars in the Galaxy.

Kilkenny et al. (1988) provided the first catalogue of spectroscopically identified hot subdwarfs which totalled 1225 sdO/Bs. Østensen (2004) compiled the first online database of more than 2300 entries largely based on surveys targeting extragalactic sources (Hagen et al. 1995; Wisotzki et al. 1996; Mickaelian et al. 2007; Mickaelian 2008). Since then, large-scale sky surveys like the Sloan Digital Sky Survey (SDSS) (Geier et al. 2015; Kepler et al. 2015, 2016, 2019), Edinburgh-Cape (EC) survey (Stobie et al. 1997), and the Galaxy Evolution Explorer (GALEX) (Vennes et al. 2011) have contributed extensively to this number using both spectroscopy and photometry. In an effort to provide an up-to-date catalogue of hot subdwarf stars, Geier et al. (2017) compiled 5613 unique sources whose classifications are based on spectroscopy and photometry from these large-scale surveys, as well as radial velocities, atmospheric parameters, and light-curve variations where available. This list has since been updated (Geier 2020; Culpan et al. 2022) in the light of the copious all-sky survey data now available, adding over 500 more objects to the catalogue of known hot subdwarfs in our Galaxy.

The main motivation behind compiling catalogues of hot subdwarf stars is to constrain evolutionary models. In this context, early determinations of their spatial distribution, based on flux-limited samples, yielded conflicting scale heights from 175 to  $\approx 1,000$  pc. This discrepancy extended to the derived space densities, varying between  $\approx 3.8 \times 10^{-7}$  to  $4 \times 10^{-6}$  stars/pc<sup>3</sup> (see Table 1 for an overview of the previous studies). In short, these previous investigations focused on specific and limited sky regions, such as the poles (Heber 1986; Saffer 1991), Galactic disk (Downes 1986; Villeneuve et al. 1995b), and intermediate latitudes (Moehler et al. 1990a; Theissen et al. 1993; Saffer 1991) of the Galaxy. Villeneuve et al. (1995a) used the entire footprint of the Palomar Green (PG) survey (Green et al. 1986). These studies, constrained by flux-limited samples, faced limitations in the maximum distances and volumes that could be studied, with notable incompleteness at bright magnitudes and misclassifications. These challenges were identified as major caveats, as pointed out by Moehler et al. (1990a) and thoroughly discussed by Villeneuve et al. (1995a). The deepest samples primarily included stars at distances typical for thick-disk stars, suggesting potential incompleteness in modern catalogues of known hot subdwarfs (Geier et al. 2017; Geier 2020; Culpan et al. 2022) at bright magnitudes. Consequently, there is a need for an all-sky survey with precise and established completeness.

Complete volume-limited samples offer ideal benchmarks for population studies with their reduced selection effects as they can be directly compared to the output of a population synthesis code. The first attempt at defining a volume-limited sample of hot subdwarf stars, to the best of our knowledge, was Stark & Wade (2003) who, using photometric data from the Two Micron All Sky Survey (2MASS) second incremental data release catalogue, corrected for the selection bias by removing those hot subdwarfs that they observed to be composite, but would otherwise not have been observed if they had been single objects. However, the sample remains to some extent magnitude-limited as no definitive volume can be drawn in this way.

Parallax measurements offer the most direct method for determining distances to nearby stars. Crucially, the *Gaia* space observatory has significantly improved the accuracy of these measurements across all declinations, allowing for the selection and cross-matching of complete all-sky samples with abundant spectroscopic data from the literature (e.g. Gaia Collaboration et al. 2021; Kilic et al. 2020). In its Early Data Release 3 (Gaia Collaboration 2020), the accuracy of astrometry was significantly improved by the extended time baseline since the previous groundbreaking Data Release 2 (DR2) (Gaia Collaboration et al. 2018a). Leveraging this progress, Culpan et al. (2022) (hereafter CG22) curated a catalogue of hot subluminescent star candidates. The selection was based on their positions in the colour-absolute magnitude parameter space in the HRD, primarily confined between main sequence stars of spectral types O and B and white dwarfs (Østensen 2006; Geier et al. 2017; Geier 2020). Moreover, the authors generated a main sequence rejection criterion to remove the millions of main sequence stars located redwards of this cut that would contaminate the sample (see Fig. 4 of CG22). Ultimately, the good parallax selected catalogue contains 13,123 candidates from which our volume-limited sample is directly drawn. In this paper we consider stars at distances closer than 500 pc as indicated by their Gaia DR3 parallaxes, which roughly corresponds to a magnitude limit of  $m_G = 12 - 14$  mag for unreddened samples, given the spread of absolute magnitudes of sdB stars (see Fig. 11). We note that fewer than 50 stars lying within 500 pc (see Table 1) were included in the early investigations, while the sample studied here is about seven times larger. This offers, for the first time, an unbiased sample which we utilise to derive the most precise estimates of the local space density and spatial number distributions of hot subdwarf stars to date.

## 2. Sample selection

### 2.1. Defining the distance limit, known candidates, and possible chance alignments

Utilising the CG22 catalogue of good parallax candidates, we began by selecting a suitable volume for a statistical study of the population. We were aiming for a balance between a sample size large enough for robust statistical analysis and observational feasibility within a few years. Choosing a volume defined by 500 pc effectively encompasses the local Galactic disk centred on the Sun. We applied a parallax threshold, accounting for the zero-point correction, as follows:

$$\omega_{zp} + 1\sigma_{\omega} \geq 2 \text{ mas.} \quad (1)$$

Here  $\omega_{zp}$  is the zero-point corrected parallax and  $\sigma_{\omega}$  is the standard error on that parallax; moreover, the parallax error takes into account the inflation factor outlined in El-Badry et al. (2021). The above corresponds to a distance limit of  $d_{\omega} \leq 500 + 1\sigma_{\text{dist}}$  pc (i.e. no farther than the distance uncertainty) and results in 584 candidate sources. The mean fractional parallax error of all sources in our sample is 5.6% which is well below the 20% threshold limit given in Bailer-Jones (2015), Bailer-Jones et al. (2018), and Bailer-Jones et al. (2021). Accordingly, we appropriate the inversion of parallaxes for all stars in this sample and adopt no prior information to improve the distance measurements.

Following this selection defined by Eq. 1, we performed an external cross-match with the latest catalogue of spectroscopically identified hot subdwarf stars (Geier 2020; Culpan et al. 2022) using TOPCAT (Taylor 2005); all 192 previously

Survey & study	Field size (deg <sup>2</sup> )	Spectral type	Brightness limit (mag) <sup>a</sup>	Number of stars	Within 500 pc (Gaia DR3)	Scale height (pc)	Space density (10 <sup>-7</sup> stars pc <sup>-3</sup> )
SB* (Heber 1986)	840	sdB	14.2(y/V)	12	6	190–220	40
KPD <sup>†</sup> (Downes 1986)	1,144	sdB/sdO	15.3(B)	31/20	1	175	20/7
KPD (Villeneuve et al. 1995b)	1,144	sdB/sdO (H-rich)	15.0(V)	25	1		3.8 ± 1.7
PG <sup>‡</sup> (Mochler et al. 1990a)	712	sdB	14.2(y)	11	5 <sup>b</sup>	250	10
PG (Theissen et al. 1993)	600	sdB	14.2(y)	11	3 <sup>b</sup>	180 <sup>+190</sup> <sub>-60</sub>	19 <sup>+32.4</sup> <sub>-13.4</sub>
PG (Saffer 1991; Saffer & Liebert 1995)	3 × 1,200	sdB	15.4(y/V)	68	19 <sup>b</sup>	285 <sup>+120</sup> <sub>-35</sub>	7.5
PG (Villeneuve et al. 1995a)	10,714	sdB/sdO (H-rich)	15(y)	209	≈ 40	600 ± 150	3 ± 1
This work	All-sky	All considered	Volume-limited	305	305	281 ± 62	6.15 <sup>+1.16</sup> <sub>-0.53</sub>

\* Slettebak & Brundage (1971)

† Downes (1986)

‡ Green et al. (1986)

<sup>a</sup> Photometric magnitudes: Strömgen *y*, Johnson *B*, *V*

<sup>b</sup> Stars also in the sample of Villeneuve et al. (1995a)

Table 1: Previous population studies of hot subdwarf stars

known sources within 500 pc were in our sample. The literature search was conducted using the SIMBAD Astronomical Database<sup>1</sup> (Wenger et al. 2000), identifying a total of 260 out of the remaining 392 candidates. These included CVs, WDs, and MS stars, all listed in Table A.3 in the appendix. However, as hot subdwarfs are notoriously misclassified as main sequence stars of spectral types O, B, or A, those without accessible or poor quality spectra in the literature were subject to follow-up spectroscopic observation.

*Gaia* has the angular resolution to distinguish sources on the sky whose fainter component would otherwise be completely blended in other spectroscopic and photometric observations. TYC8357-3863-1 is one such case identified where the proximity of HD 165493, an apparently nearby bright star, has hindered the acquisition of a spectrum. Coronagraphy may assist in isolating this system. No other chance alignment was identified in this sample.

## 2.2. Further cleaning

The release of *Gaia* DR3 has provided new astrometric quality control parameters that enable sources with unreliable astrometric solutions to be identified. The *astrometric\_excess\_noise* (AEN) (see Lindegren et al. 2012, for details on the astrometric modelling) and the re-normalised unit weight error (RUWE)<sup>2</sup> are two such commonly used parameters and are recommended by the *Gaia* Data Processing and Analysis Consortium (DPAC) to be < 1.0 and < 1.4, respectively.

We find that these thresholds are not appropriate in our selection, as many known hot subdwarf stars drastically exceed these limits. Of our selected 500 pc candidates, 215 sources (37%) have RUWE and AEN assignments far larger than these criteria as shown in Fig. 1. Binary systems, in which many hot subdwarfs reside, may induce a photocentric wobble that is problematic for *Gaia*'s single-star astrometry model, resulting in an inflation of these values (Lindegren et al. 2018; Belokurov et al. 2020; Penoyre et al. 2022; Lindegren et al. 2021). Of the identified hot subdwarf stars in our sample, those hosting main sequence companions appear to facilitate the largest RUWE values up to 5.55, which is a tangible outcome as both constituents are of similar

brightness. WD companions seem to have little impact by comparison.

For the cleaning of our catalogue, we adopt a relaxed limit of  $\text{RUWE} < 7$  as indicated by the red dashed line which excludes 205 sources from our sample. This limit was chosen as it does not remove any spectroscopically confirmed hot subdwarf stars and is in the interest of arriving at a criterion that defines a sample that is both as clean and complete as possible.

The impact of this selection is evident in Fig. 2, showcasing *Gaia* CMD's in the top panels and skyplots in the bottom panels. All candidates from CG22, selected using Eq. 1, are depicted. Those with RUWE values exceeding 7 are highlighted red. Notably, many of these sources cluster near the MS of the CMD between 0.3 and 0.4 BP-RP, as well as in a specific region in the Galactic mid-plane at a longitude of  $\approx 120$  degrees. If genuine, such behaviours are unexpected, as the impact of interstellar extinction is unlikely to play a significant role in this selection (refer to Sect. 6 for detailed discussion). A 500 pc sample should demonstrate a roughly homogeneous distribution across the sky, as confirmed by a statistical test of homogeneity (see Sect. 4.2). Twenty-one sources with  $\text{RUWE} > 7$  are identified as MS stars based on spectra in the LAMOST DR8 database. It is highly probable that the majority of these spurious sources result from contamination in crowded fields. The application of our adopted criterion,  $\text{RUWE} < 7$ , effectively eliminates these dense star concentrations, yielding a clean and homogeneously distributed sample shown in the right panels of Fig. 2, which serves as the basis for this study.

A comparable pattern was observed in sources from a 500 pc sample initially sourced from Geier et al. (2019), which, in turn, utilised *Gaia*'s DR2 (Gaia Collaboration et al. 2018b). This initial sample comprised 635 candidate sources, with 70% necessitating spectroscopic identification. The ongoing spectroscopic follow-up campaign, conducted since 2019, yielded the majority of spectra utilised for spectral classification. The release of *Gaia*'s DR3, featuring an extended base line, provided updated astrometric data with fewer outliers. In Fig. 3, a *Gaia* CMD pair-plot showcases the original 500 pc sample of 635 hot subluminoous star candidates. The pair-plot (illustrated with dotted lines) visually depicts the shift these sources experienced in this parameter space due to the updated parallaxes and apparent magnitudes of DR3, with the circle indicating the DR3 data. Notably, many sources near the MS rejection criterion of CG22 (depicted by the dashed line) underwent a significant vertical shift, with the

<sup>1</sup> <https://simbad.u-strasbg.fr/>

<sup>2</sup> Details on the RUWE can be found in the document "Re-normalising the astrometric chi-square in *Gaia* DR2" and is available at: <https://www.cosmos.esa.int/web/gaia/public-dpac-documents>

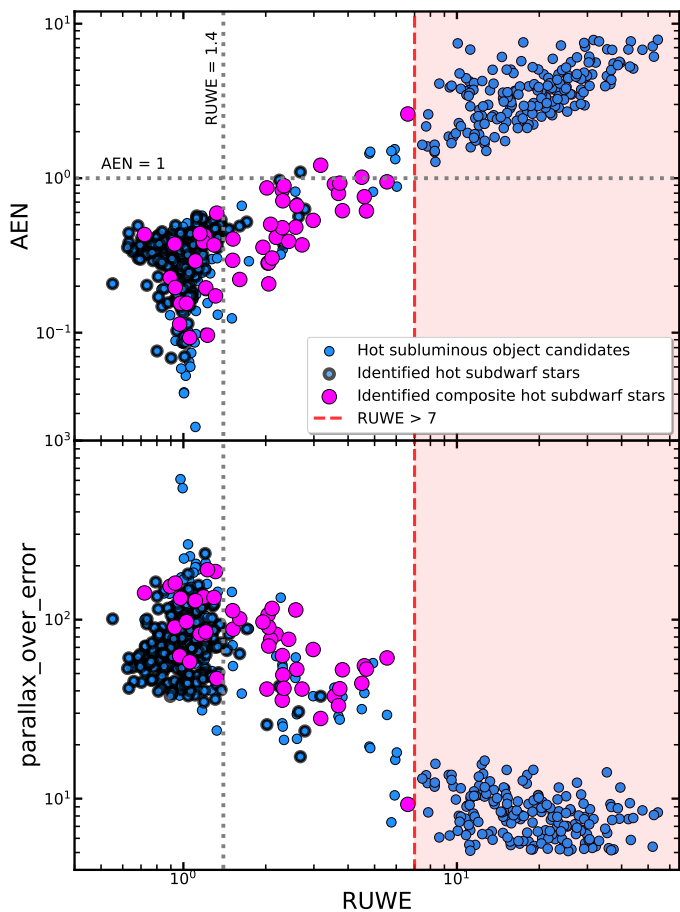


Fig. 1: Plot depicting the distribution of the 584 candidate hot subluminal stars within 500 pc (blue) for three astrometric quality control parameters provided by *Gaia* DR3. Top panel: AEN vs RUWE where all currently known hot subdwarf composite and non-composite binaries are given as magenta and black circles, respectively. The dashed grey horizontal and vertical lines indicate an AEN of 1.0 and a RUWE of 1.4, respectively. The red dashed line and the corresponding red shaded area represent the rejected sources in the sample. Bottom panel: Same as top, but with `parallax_over_error` vs RUWE.

red circles indicating those possessing RUWE values larger than 7. Through our extensive follow-up spectroscopic campaign, we determined that 295 (99%) of these removed sources are MS stars located in crowded fields near the Galactic plane. The revised astrometry from *Gaia*'s DR3 now places all these sources well beyond 500 pc. In this paper, we consider this evidence sufficient to confidently establish a limit in RUWE for the cleaning of the 500 pc sample, particularly for those sources now sourced from *Gaia*'s DR3. It is important to emphasise, however, that no single, uniform selection criterion can be universally applied across the sky due to the intrinsic limitations of *Gaia*, such as challenges in crowded fields, which cannot be encapsulated by a single threshold in all situations. We underscore that our selection criteria are specifically tailored for this sample, and any adopted quality control criteria should be chosen appropriately for each unique selection of stars from the *Gaia* database.

Lastly, a handful of targets were also removed and were not subject to follow-up spectroscopic observation and are instead listed in Table A.3 and indicated as removed sources. These sys-

tems were either in close proximity to the spurious region of our data in Fig. 2 and still possessed high RUWE values, or were deemed too bright to be genuine hot subdwarf stars.

### 3. Observations, data reduction and classification

#### 3.1. Spectroscopy

Over two-thirds of the *Gaia* DR2 500 pc sample were primarily based on colour and absolute magnitudes, triggering a spectroscopic follow-up campaign that observed over 400 hot subdwarf stars between 2019 and 2021. Observations were carried out from a variety of telescopes and instruments including the INT/IDS,<sup>3</sup> NOT/ALFOSC,<sup>4</sup> NTT/EFOSC2,<sup>5</sup> SOAR/Goodman,<sup>6</sup> and CAHA 3.5m/PMAS<sup>7</sup> and targeted the optical sector between 3300 Å and 7400 Å where a high signal-to-noise of at least 50 was obtained for each star which is suitable for classification and a detailed line profile analysis. A summary of the observations is presented in Table 2, which covers a total of 34 nights where some targets were observed more than once. In addition, high-quality spectral classifications for 322 of our target candidates were provided, which stem from a low-resolution survey conducted at the B&C spectrograph on the University of Arizona 2.3m Bok telescope. For a description of this dataset, see Green et al. (2008).

The spectroscopic data obtained by follow-up observations were reduced and analysed using PyRAF procedures (Science Software Branch at STScI 2012), a command language for the IRAF (Tody 1986) (Image Reduction and Analysis Facility) which is a general purpose software developed by the National Optical Astronomy Observatories (NOAO) using the longslit package for 2D spectroscopic images. This included basic bias and flat-field corrections, wavelength calibrations, and flux calibrations of the instrument response function with atmospheric extinction taken into account.

#### 3.2. Archival data

Online databases provided the remaining spectroscopic data. The Large Sky Area Multi-Object Fiber Spectroscopic Telescope DR7 (v.2) (LAMOST; Luo et al. 2022) low-resolution spectroscopic survey (LRS), and its more recent DR8, provided 151 quality spectra covering wavelengths up to 9100 Å. The European Southern Observatory (ESO) archive<sup>8</sup> and the Mikulski Archive for Space Telescopes (MAST)<sup>9</sup> were also searched and yielded several high-resolution spectra for stars in our sample which will be utilised for accurate atmospheric parameters. None of our selected targets are found in the archives of the Sloan Digital Sky Survey (SDSS) because they are brighter than the bright magnitude limit for this survey.

#### 3.3. Hot subluminal star classification

Our classification of hot subdwarf stars is based on the scheme outlined in Moehler et al. (1990b), which is updated and extended in CG22. Figure 4 displays example spectra illustrating

<sup>3</sup> <http://www.ing.iac.es>

<sup>4</sup> <http://www.not.iac.es/instruments/alfosc/>

<sup>5</sup> <https://www.eso.org/public/teles-instr/lasilla/ntt/efosc2/>

<sup>6</sup> <https://noirlab.edu/public/programs/ctio/soar-telescope/goodman/>

<sup>7</sup> <https://www.caha.es/CAHA/Instruments/PMAS/pmas.html>

<sup>8</sup> [http://archive.eso.org/eso\\_archive\\_main.html](http://archive.eso.org/eso_archive_main.html)

<sup>9</sup> <https://archive.stsci.edu/>

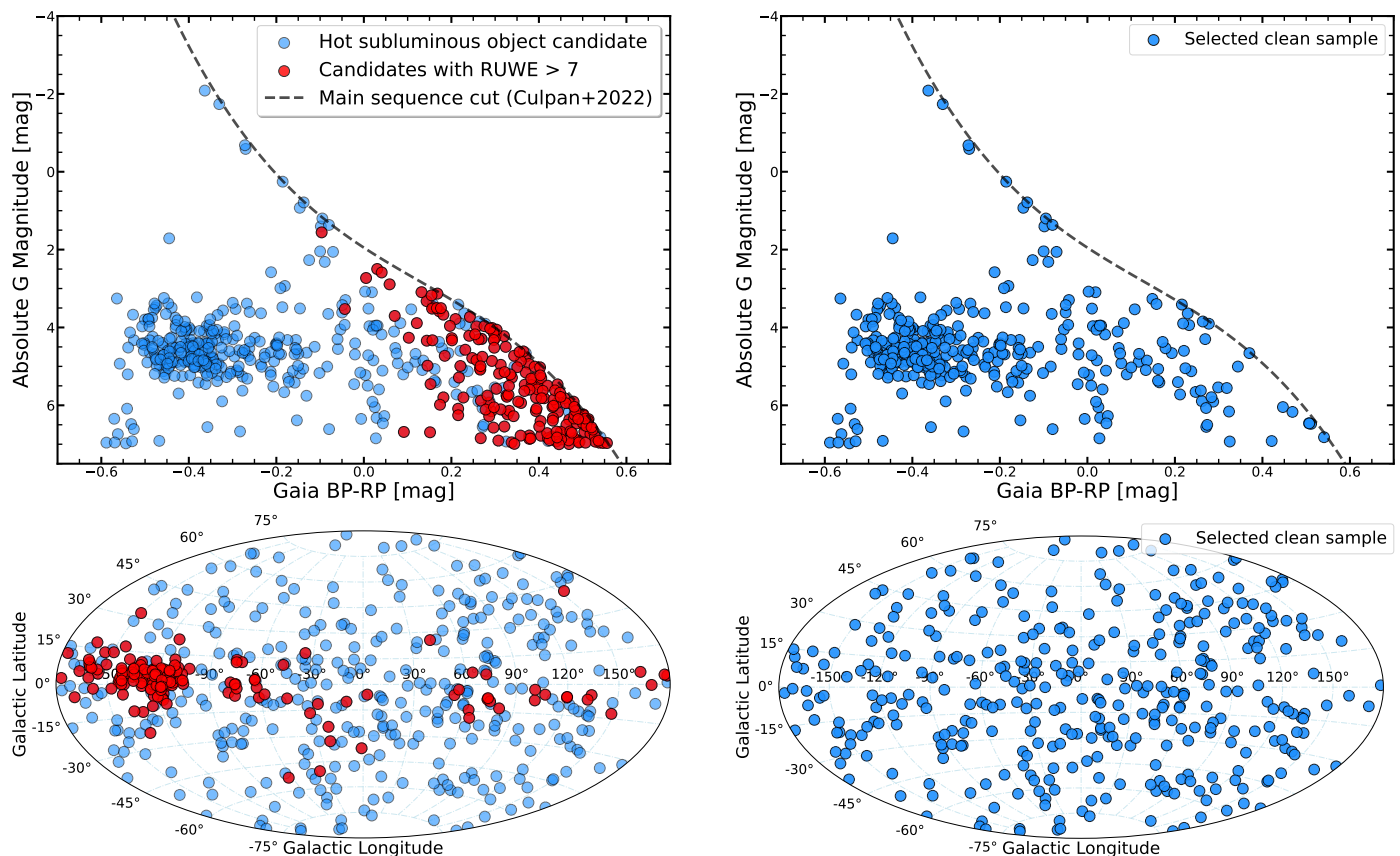


Fig. 2: *Gaia* colour-magnitude diagrams and sky distributions of the 584 candidate hot subluminous stars within 500 pc drawn from *Gaia* DR3. Those candidates with RUWE values in excess of 7 are indicated by red circles and have been removed in the panels on the right, which display the cleaned sample that was adopted. The exclusion of sources with  $\text{RUWE} > 7$  resulted in a reasonably homogeneous sky distribution given in the bottom right panel as expected for a 500 pc sample.

Telescope/Instrument	Stars observed	Set-up	Wavelength range [ $\text{\AA}$ ]	Spectral resolution ( $\Delta\lambda$ [ $\text{\AA}$ ])	Programme ID
INT/IDS/EEV10	140	R400V	3300 - 7400	4.2	ING.NL.19B.005 ING.NL.20A.003
NOT/ALFOSC	13	Grism 18	3450 - 5350	4.4	60-503
NTT/EFOSC2	173	Grism 7	3270 - 5240	7.4	0103.D-0511(A) 0104.D-0514(A) 0105.D-0121(A) 0106.D-0188(A) 0103.D-0530(A)
SOAR/GOODMAN	29	400 1 mm <sup>-1</sup>	3300 - 7050	2.97	2019B-012 2021A-008 2022B-966788 C057 CN2020A-87 CN2020B-74 CN2021A-52
CAHA 3.5m/PMAS	11	V600	3600 - 6800	3.63	GTO
Other					Source
LAMOST DR8	151	LRS	3690 - 9200	3.05	Database query
Literature parameters	149				Culpan et al. (2022)

Table 2: Overview of the spectroscopic data

this scheme. We emphasise that the classifications in this work are primarily based on visual inspection of available or obtained spectra, or otherwise reliable literature classifications.

In addition to this scheme, hot subdwarf stars may display signatures of cool companions in the spectrum. We take the  $G$ -band absorption as a clear companion signature, as well as the

Mg I triplet at 5167  $\text{\AA}$ , 5173  $\text{\AA}$ , and 5184  $\text{\AA}$ . The photometric signatures of composite-colour hot subdwarf stars are described in detail in Sect. 5.3 where the construction of spectral energy distributions are employed to detect cool MS companions. This is necessary since companions of type K may be too dim to be seen in an optical spectrum, whereby the SED method then becomes

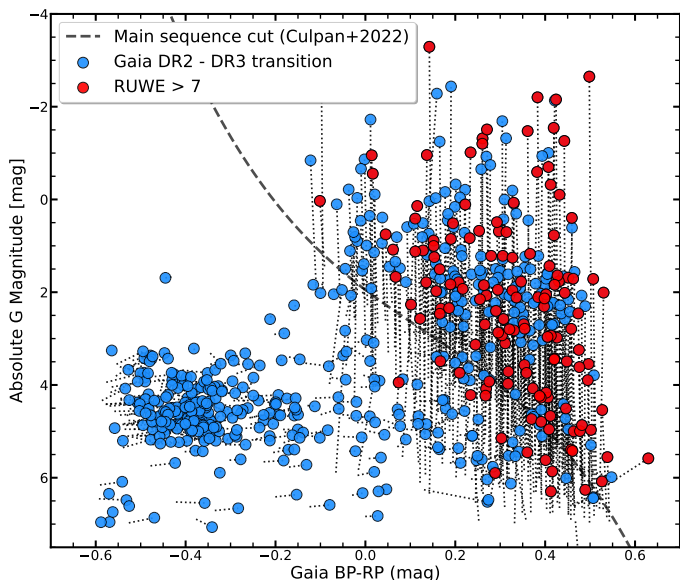


Fig. 3: Colour-magnitude diagram of hot subluminal star candidates originally selected from Geier et al. (2019), which draws from *Gaia* DR2. The plot highlights the impact the updated parameters in the *Gaia* DR2 to *Gaia* DR3 transition had on the flagship 500 pc sample. The pair-plot shows the shift each star underwent after DR3 where the circle represents the DR3 data. The vertical shift near the MS stems primarily from the improved astrometric solution.

the only option to detect the companion in the infrared if the photometric data is available.

As was introduced in CG22 to compliment the spectroscopic classes sdB, sdOB, sdO, and He-sdB/OB/O, we also consider the spectral classes O(H), O(He), PG1159, and [WR] to classify the hotter central stars of planetary nebulae (CSPNe) and other post-AGB stars found in our parameter space. In addition, this region in the HRD has been found to also contain cooling progenitors of helium WDs such as HD 188112 (Heber et al. 2003). These stars may be spectroscopically indistinguishable from sdB stars, as is the case for HD 188112. However, they may also display spectral features similar to MS A-type stars that is void of any helium such as [PS72]97, a recently identified helium WD progenitor that is present in our sample (Kosakowski et al. 2023). We use the sdA class to distinguish this population.

Lastly, we use the spectral classes of WD, CV, MSB/A/F, and BHB in order to fully classify our sample where no known spectroscopic classes are otherwise available in the literature. The last two are often indistinguishable using low-resolution spectra. For this population, we combine our obtained spectra with SED fits (Sect. 5.3) to obtain the radius and approximate masses of these stars to distinguish them.

This scheme is adopted in an attempt to comprehensively and homogeneously account for all the populations found in this parameter space. A detailed analysis of the subpopulations of hot subdwarf stars will be explored in a future paper to disentangle the various evolutionary histories.

## 4. Analysis

### 4.1. Spatial distribution, space density and scale height

Following the spectral classification by visual inspection, we explore potential relationships between the classes of hot subluminal stars and their Galactic positions. Previous studies faced challenges from complicated selection biases in magnitude-limited surveys or were constrained to specific sky regions, especially for hot subdwarfs (e.g. Heber 1986; Downes 1986; Villeneuve et al. 1995a,b) (see Table 1 for an overview). The sky plots on the left in Fig. 5 reveal a relatively homogeneous distribution of hot subdwarf stars (top left panel) and other constituents like CVs (bottom left panel) across the sky, irrespective of spectral class. On the right, we project the sample onto the Galactic Z-R and Y-R planes; the hot subdwarfs again exhibit a homogeneous distribution in 3D space, with a small void of stars in the upper right quadrant, possibly indicative of Galactic structure (see Sect. 4.2). A tendency for stars to concentrate near the Galactic plane suggests a decreasing space density with Galactic height. CVs, in contrast, show indications of scarcity towards the Galactic centre, while WDs are nearly absent on one hemisphere. These systems, primarily located in the lower right corner of the CMD (see Fig. 11 in Sect. 5), are more likely to be removed from our selection due to interstellar extinction.

It is often assumed that the vertical density profile of the Galaxy at the solar radius can be described in the same way as the radial profile, a simple exponential barometric distribution for various kinds of stars (e.g. Kroupa 1992; Jurić et al. 2008; Bovy et al. 2012, 2016; Pala et al. 2020; Schaefer 2022), which would then take the form:

$$\rho = \rho_0 e^{-|z|/h_z} \quad (2)$$

where  $h_z$  is the exponential scale height,  $z$  is the distance in parsecs from the Galactic mid-plane,  $\rho$  is the density at distance  $z$ , and  $\rho_0$  is the density at  $z = 0$ . However, there are currently two main geometric contenders of the  $z$ -profile, the second being a hyperbolic secant, which takes the following form:

$$\rho = \rho_0 \operatorname{sech}^2\left(\frac{|z|}{h_0}\right) \quad (3)$$

where  $h_0$  is the vertical characteristic height of a self-gravitating, locally isothermal sheet (Spitzer 1942; van der Kruit & Searle 1981a,b). This profile essentially combines a Gaussian at small distances around the mid-plane with a barometric exponential at large distances and is in popular use (e.g. Gilmore & Reid 1983; Villeneuve et al. 1995a,b; Bilir et al. 2006; Yoachim & Dalcanton 2006; Widrow et al. 2012; Ma et al. 2017; Canbay et al. 2023). To facilitate comparison with other literature values, we take the approximation of this function at  $|z|/h_0 \gg 1$  where it asymptotes to resemble an exponential with a scale height  $h_z = h_0/2$ . While other forms of this model, such as *sech*, exist, we do not explore them here due to their minimal impact on describing the plane's flattening with the relatively small number of stars in our sample. Multiple components are often employed to acquire more precise descriptions of the data, especially to account for multiple Galactic populations. Given the reported scale heights of the Galactic thin and thick disk (300 pc and 900 pc, respectively, according to Jurić et al. (2008)), we adopt a straightforward approach, mapping the  $z$ -axis density variation using a single component. We use both a hyperbolic secant (eq. 3) and an exponential (eq. 2) as two-parameter fits for  $\rho_0$  and  $h_z$

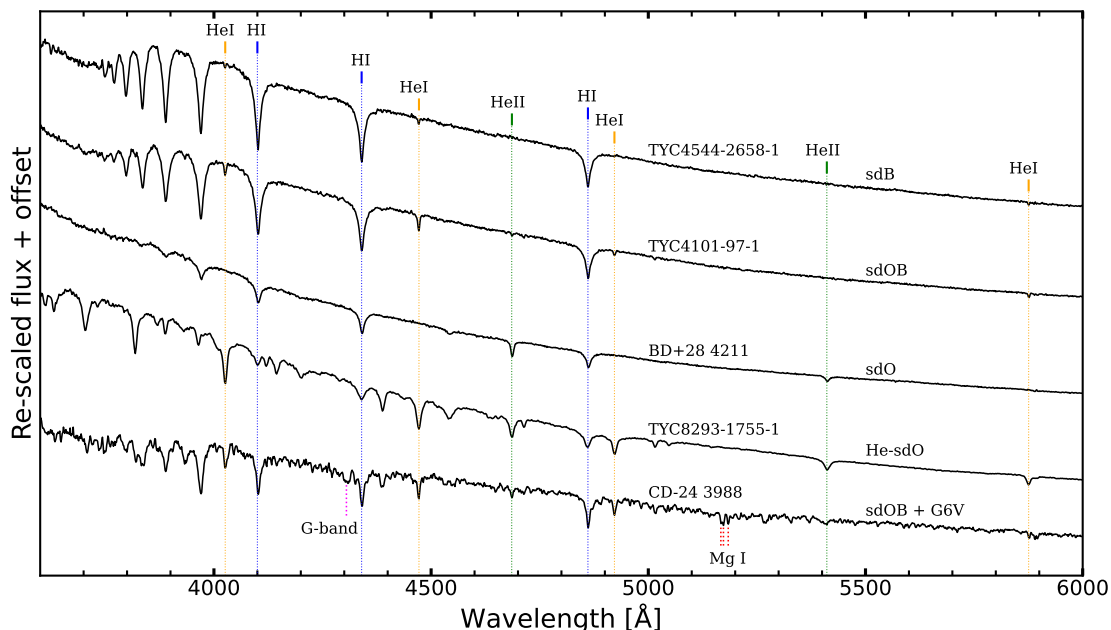


Fig. 4: Example identification spectra obtained in this study to illustrate the adopted classification scheme and to showcase the high quality of the dataset. The primary diagnostic lines of He I, He II, H I, the Mg I triplet, and the G-band are marked in gold, green, blue, red, and magenta respectively. These spectra were obtained at the INT and at SOAR (see Table 2).

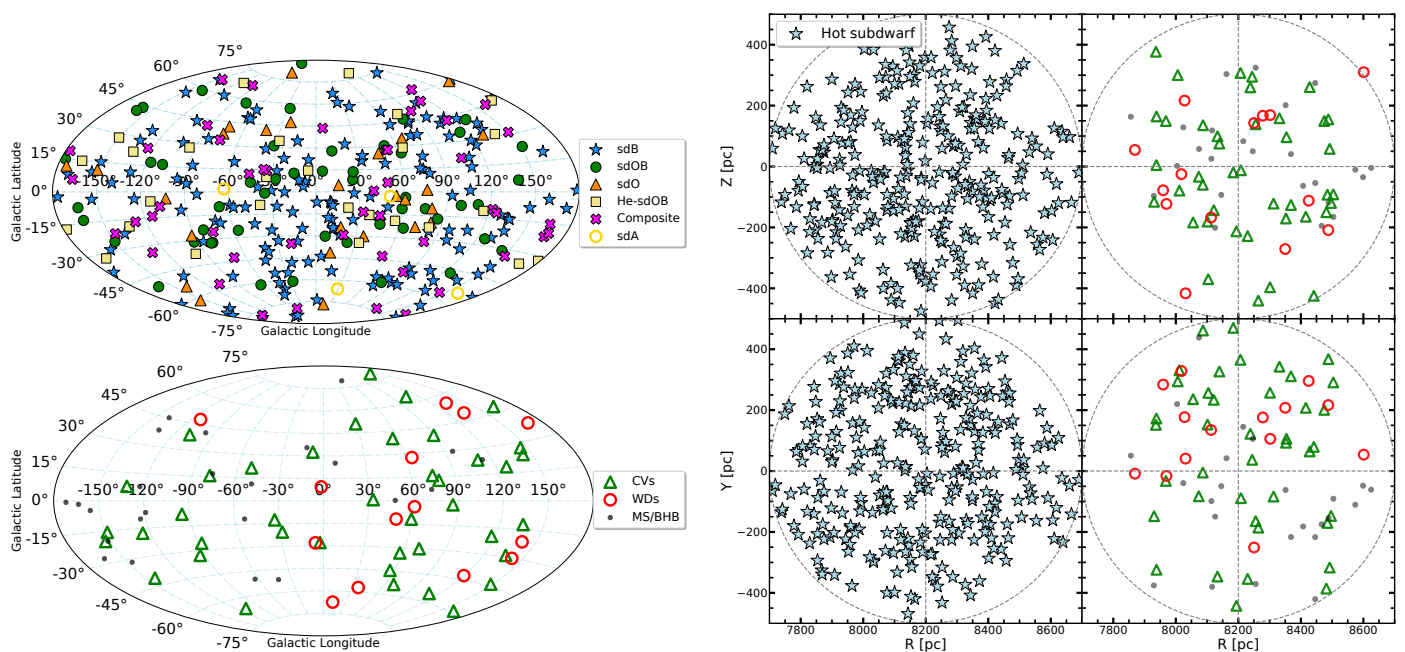


Fig. 5: Galactic distribution of the 500 pc sample and its constituents, which are labelled accordingly for all plots. The left panel describes the projected distribution of the sample on the sky in terms of Galactic longitude and latitude, whereas the right panel gives the projected positions onto the Galactic plane ( $X - Y$  plane) and on the plane perpendicular to it ( $X - Z$  plane). Here the  $X$ -coordinate is given in terms of  $R$ , the solar distance from the Galactic centre.

and compare the results. The Galactic scale length is not considered here, as the density variation along the Galactic  $x$ -axis is less than 25% on the scale of 1 kpc at the solar radius (Binney & Tremaine 1987), and very few of our stars are located at the extremities of our sample as projected onto the  $x$ -axis.

We focus initially on the non-composite hot subdwarfs, constituting the primary population in our sample with 257 members (table A.1). Composite-colour hot subdwarfs are excluded from this analysis due to known incompleteness, which could introduce bias (see Sect. 6 for a discussion on the completeness of this population). The sample is divided into equally spaced bins along the  $z$ -axis. To increase number statistics, we consider

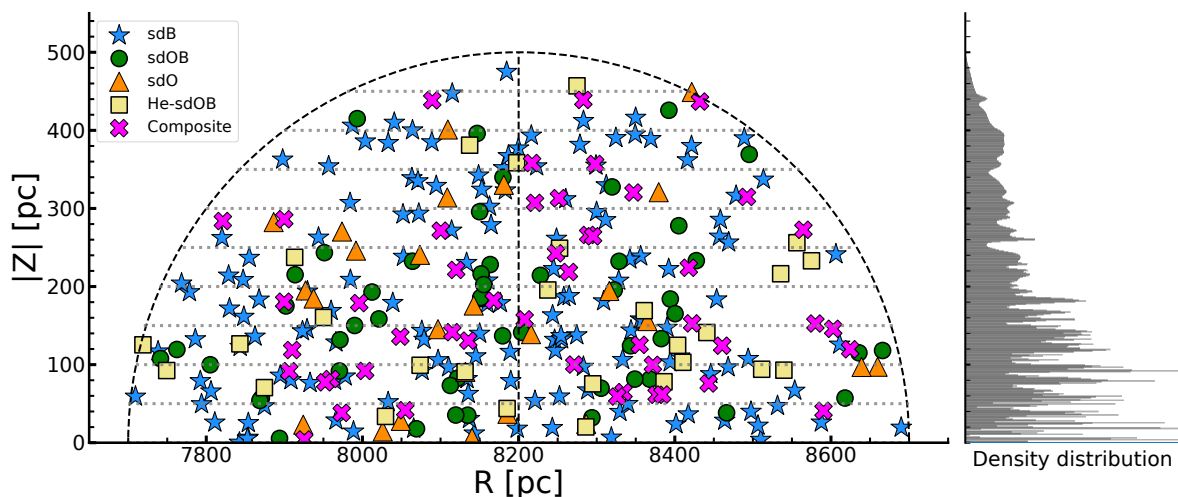


Fig. 6: Projected distribution of the 500 pc sample above the Galactic plane. Left panel: 500 pc sample is projected onto the R-|Z| plane with the different classes of hot subdwarfs colour-coded accordingly. The black dashed line indicates the 500 pc distance limit, whereas the horizontal grey dashed lines represent a 50 pc binning example for how the sample has been divided up to derive the scale height. Right panel: Positional probability density distribution projected onto the  $z$ -axis taking the standard parallax errors of *Gaia* into account - displayed as a stacked histogram.

the absolute value of the  $z$ -component of each star, essentially doubling our sample, as illustrated in Fig. 6. The component  $z$ , denoted as  $z = d \sin(b)$ , incorporates the Galactic latitude  $b$  and the distance  $d$  of each star. The solar offset to the Galactic plane is not considered in this analysis due to its omission from the selection criteria, and its determination is not confident with the limited stars in our sample. We generate arrays of distances using scalar parallax measurements from *Gaia*, along with the inflated parallax uncertainties (El-Badry et al. 2021), employing a Monte Carlo approach. These distances are projected onto the  $z$ -axis, forming distance probability distributions (see the right panel of Fig. 6 for a stacked histogram of these distributions). The smoothing in the distribution, reflecting increasing parallax errors with distance, is evident. This procedure accounts for the non-linearity of parallax inversion, especially near the sample boundary or between bins, where stars contribute with varying weights due to distance uncertainties. The probability arrays for each bin provide the number of stars and uncertainties, determined by means and standard deviations, respectively. Calculating densities for each bin involves dividing these numbers by the corresponding volumes of each slice,  $V_{slice}$ , determined using the equation:

$$V_{slice} = \frac{1}{6} \pi h (3R_1^2 + 3R_2^2 + h) \quad (4)$$

where  $h$  is the width of the spherical segment or bin width and  $R_1$  and  $R_2$  are the radii of the top and base of the circle segment.

We employed a non-linear least-squares algorithm (Python library LMFIT) to simultaneously fit the scale height and mid-plane density, as given by equations 2 and 3. Errors were obtained from the estimated covariance matrix during the fit. Our analysis indicates that the  $\text{sech}^2$  provides a much better description of the data, especially around the Galactic mid-plane. An exponential fit, on the other hand, performs well when modelling beyond 100 pc along the  $z$ -axis. However, attempting to model all data points results in a systematic inclination for the fitting procedure to choose excessively large scale heights ( $h_z \geq 1000$  pc). This reflects a smooth profile at  $z \leq 100$  pc. The implications

of this tendency are unclear; it could, although unlikely, signify the true physical morphology of the local thin disk or imply a significant number of missing stars in the mid-plane, warranting further investigation.

The number count versus  $z$  is shown in the top panel of Fig. 7 for the median bin sizes of the fitting routine described below, with the corresponding density profile provided in the lower panel. A notable feature in this plot is a peak between 300 and 400 pc, which probably arises from the rapidly decreasing bin volumes along the along the  $z$ -axis.

However, vertical wave-like features in the number counts that run parallel to the Galactic disk have been corroborated in several studies (Widrow et al. 2012; Yanny & Gardner 2013; Ferguson et al. 2017; Xiang et al. 2018; Bennett & Bovy 2019). Widrow et al. (2012) found peaks in the stellar number density at around  $Z \approx -400$  and 800 pc for the solar neighbourhood, which are asymmetrically reflected around the Galactic plane, and is reportedly strongest for the youngest populations in the more recent work by Xiang et al. (2018). These findings are in reasonable agreement with our local population of hot subdwarf stars, particularly the peak at  $Z \approx -400$  pc (see Fig. 8).

Due to the number fluctuations, the choice of bin size for our  $z$ -profile fits introduces a relative uncertainty on the resulting scale height of up to 25% and up to 10% on the mid-plane density. To address this, we perform two parameter fits on the scale height and mid-plane density using a hyperbolic secant profile for all integer divisors of 500 between and including 5 and 20, which corresponds to bin widths between and including 100 pc and 25 pc, respectively. Attempting to fit bin widths outside of this range results in either empty bins with large fluctuations or too few data points for the fit, respectively. Along with the statistical errors from each fit propagated through from the estimate covariance matrix, we also incorporate Poisson uncertainties in quadrature. This approach accounts for the parallax uncertainties of the individual objects in our sample and the statistical variations due to the limited sample size. Poisson errors for the mid-plane densities are calculated with the following:



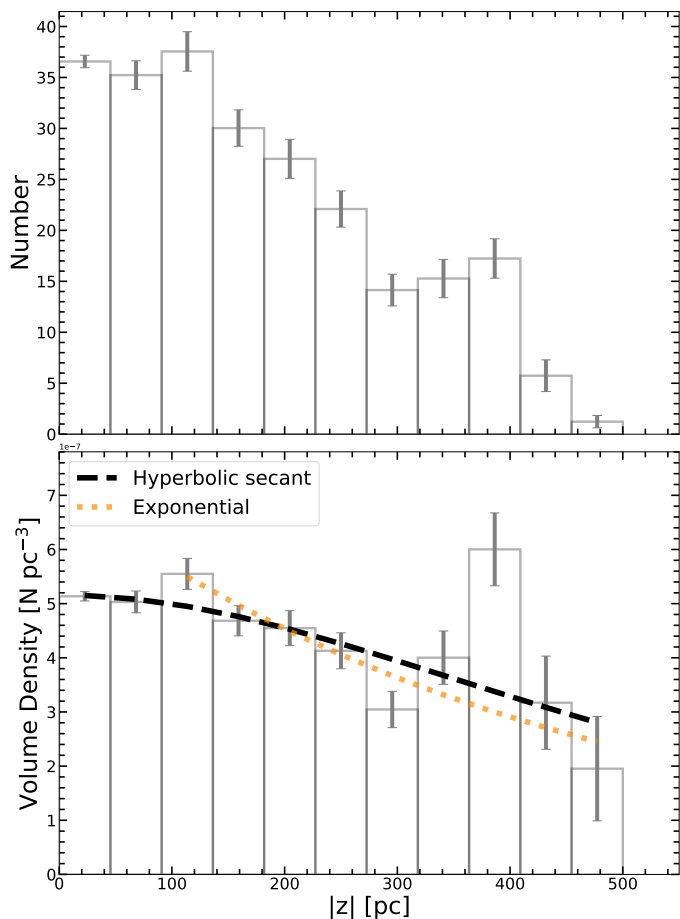


Fig. 7: Distribution of the non-composite hot subdwarf stars over the perpendicular distance to the Galactic plane,  $|z|$ . The top panel gives the number count, whereas the bottom panel displays the volume density. Median bin sizes of the fitting routine are displayed. Example fits of a hyperbolic secant profile (black) and an exponential (gold) are shown; the latter has only been fit for  $|z| > 100$  pc. The error bars are generated from the standard deviations of the positional probability distributions.

$$\sigma_{\text{Poisson}} = \frac{\sqrt{N}}{V_{\text{eff}}} \quad (5)$$

where  $N$  is the number of stars in our sample and  $V_{\text{eff}}$  is the effective volume of our sample given by Eq. 7. Poisson errors are not calculated for the scale height, as we assume the distributions of each possible sample to be the same. By fitting all possible equally spaced bins, we find an average scale height and mid-plane density of  $h_z = 281 \pm 62$  pc and  $\rho_0 = 5.17 \pm 0.33 \times 10^{-7}$  stars/pc<sup>3</sup>, respectively, for the non-composite hot subdwarf stars in our 500 pc sample. This suggests a primarily younger thin-disk population, with non-composite hot subdwarfs making up  $84.1_{-1.9}^{+2.3}\%$  of the sample, assuming binomial uncertainties. To ensure that this is representative of the full population of hot subdwarfs in our sample, we then incorporate all known composite-colour hot subdwarfs within 500 pc. This inclusion raises the mid-plane density to  $\rho_0 = 6.15_{-0.53}^{+0.55} \times 10^{-7}$  stars/pc<sup>3</sup>. The errors in this density calculation are determined by propagating standard errors on parallax measurements, Poisson uncertainties (as given by Eq. 5), and binomial uncertainties on the fraction

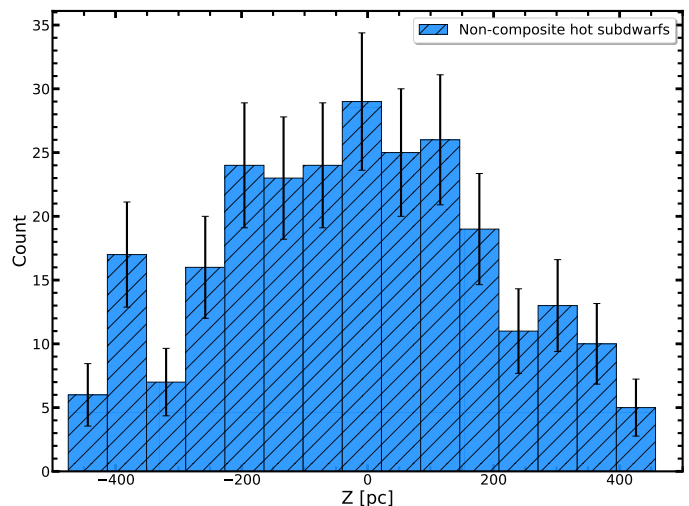


Fig. 8: Number histogram of  $z$ -distances for the non-composite hot subdwarfs around the Galactic plane.

of non-composite hot subdwarf stars in our sample. We assume that the composites share the same characteristics as the non-composites and are distributed similarly in 3D space, maintaining the scale height. The final mid-plane density calculation includes an asymmetric upper error bar, accounting for the estimated number of missing composite hot subdwarfs in our sample (as discussed in Sect. 6). Consequently, the revised mid-plane density is  $\rho_0 = 6.15_{-0.53}^{+1.16} \times 10^{-7}$  stars/pc<sup>3</sup>.

#### 4.2. A test of a uniform distribution

To evaluate the statistical significance of the local density fluctuations observed in our sample, we employ the Kolmogorov-Smirnov (KS) test to assess its homogeneity. Additionally, this test helps discern whether the scale height is the primary factor contributing to the decline in density along the  $z$ -axis. In their fifth catalogue of nearby stars, Golovin et al. (2023) utilised the KS test to evaluate the completeness of their 25 pc sample by comparing the empirical Cumulative Distribution Function (CDF) to an analytical CDF given by:

$$\text{CDF}(r) = \frac{r^3}{R_0^3}, \quad 0 \leq r \leq R_0 \quad (6)$$

where  $R_0$  is for a sphere of radius 25 pc in their case. A deviation from homogeneity implied the completeness limit at that magnitude. As our 500 pc stars are relatively bright, our sample does not suffer this magnitude limitation. We followed a similar approach and compared the CDF of the full sample of hot subluminous stars to the CDF of that given by Eq. 6 for  $R_0 = 500$  pc and performed a KS test over 5 pc intervals to test for homogeneity. Attempting to use subsamples in this analysis, such as the confirmed non-composite hot subdwarf stars as was done in Sect. 4.1, results in unreliable measurements as low-number statistics begins to dominate. The results of this effort are given in Fig. 9 as a blue line. A high  $p$ -value for distances between 100 and around 350 pc is seen, beyond which it begins to drop and suggests a deviation from homogeneity which is in reasonable agreement with our determined scale height. This becomes statistically significant at a distance of 440 pc where it reaches the  $p = 0.05$

threshold. We now follow the prescription of [Inight et al. \(2021\)](#) and define the effective volume  $V_{\text{eff}}$ :

$$V_{\text{eff}} = \int_0^R \int_{-\sqrt{R^2-x^2}}^{\sqrt{R^2-x^2}} (2\pi x) \operatorname{sech}^2\left(\frac{|z|}{2h_z}\right) dz dx \quad (7)$$

where  $x$  points in the direction of the Galactic centre,  $z$  is perpendicular to the Galactic plane, and  $h_z$  is the scale height along the  $z$ -axis. For a decreasing scale height, Eq. 7 yields an increasing volume with respect to a simple spherical volume defined by  $4\pi R^3/3$ . Using Eq. 7, we can correct for the scale height along the  $z$ -axis by adopting our determined value of 281 pc for  $h_z$ . In doing so, the same KS test then results in the red line displayed in Fig. 9. This time, the empirical CDF of the sample appears to remain homogeneous at all distances and is statistically indistinguishable from the analytical CDF at the 5% level. The slight dip present at around 450 pc could reflect an under- or overdensity at this distance or specifically the small void seen in Fig. 5 in the upper right quadrant in the Z-R and Y-R planes. However, we must be careful when interpreting this result, as the sample selection in CG22 is not straightforward and the inclusion of other low-luminosity stars such as CVs and WDs may bias the result. Yet, as the sample appears to be homogeneous overall, this rules out any major systematic selection effects or biases for our clean selection of stars and is a striking result given the relatively few stars in our sample spread across a large volume. Moreover, it reinforces our determined scale height as being the dominant contributor to the variation in spatial distribution across the 500 pc sample where the local under- and overdensities can be interpreted as statistically insignificant.

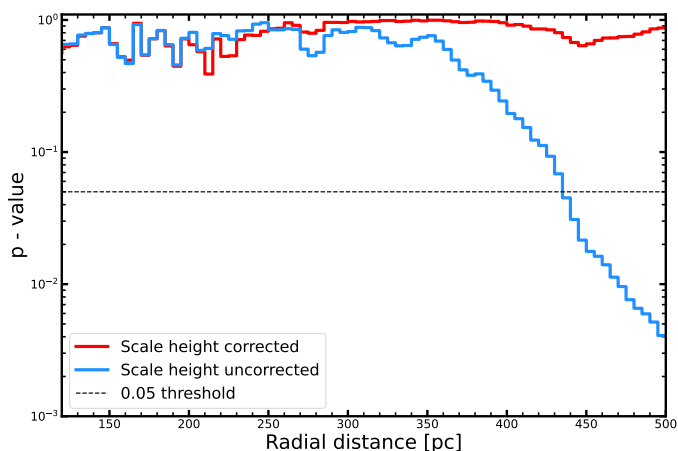


Fig. 9: Plot displaying the determined p-value as a function of radial distance at 5 pc intervals from the KS test. The blue line gives the first iteration and displays a deviation from homogeneity around 350 pc, whereas the red line gives the second iteration when the scale height is taken into account and remains high, suggesting homogeneity.

Finally, in addition to these tests over distance, we use the KS test to probe the overall homogeneity of the non-composite hot subdwarfs in the sample. We generate 1000 mock samples when taking the scale height into account where it has a distribution of distances according to:

$$r = R_0 y^{a/3} \quad (8)$$

where  $y$  is a random number between 0 and 1, and  $a$  describes a correction factor for the scale height. Each sample thus represents a distribution of distances for which we can randomly draw a number of objects from to compare to the empirical CDF of our non-composite hot subdwarfs. We then randomly draw 257 data points from each mock sample and perform the KS test, which yields an average p-value of 0.3. This implies that this population is statistically homogeneous overall and that no major selection bias is in effect.

### 4.3. Kinematics

A measurement of the scale height provides insights into the age of a stellar or substellar population, with a steeper scale height generally yielding a higher mid-plane density, inferring a younger population. However, most hot subdwarfs lack age information due to strong diffusive effects in their atmospheres, rendering metallicity an unreliable age indicator. Instead, we can examine the kinematical properties of a stellar population, which is also linked to their age. Older stars tend to have larger kinematic dispersions than younger stars ([Bovy 2017](#); [Sanders & Das 2018](#)). Utilising the accurate proper motion measurements from *Gaia*, we calculate tangential velocities, which serve as proxies for dynamical heating, using the following formula:

$$V_T = \frac{4.74}{\omega_{zp}} \times \sqrt{\mu_{\text{RA}}^2 + \mu_{\text{DEC}}^2} \quad (9)$$

where  $\omega_{zp}$  is the zero-point corrected parallax,  $\mu_{\text{RA}}$  and  $\mu_{\text{DEC}}$  are the *Gaia* proper motion measurements in right ascension and declination respectively, and 4.74 is a unit conversion factor to give the tangential velocity  $V_T$  in km/s. Figure 10 displays the distribution of tangential velocities as a histogram, where confirmed hot subdwarfs are shown in blue, and the remaining objects in the sample are grey. Both sets exhibit a similar distribution, indicating the absence of outstanding contamination arising from highly underestimated distance measurements in the Galactic plane, which was observed in DR2. Four stars in the sample have tangential velocities exceeding 200 km/s, as determined from *Gaia*'s proper motion measurements. These include three known hot subdwarf stars: LSIV –14 116 (He-sdOB), Feige 46 (He-sdOB), and SB744 (sdOB+F/G). The fourth star, TYC144-2049-1, is a BHB star candidate according to [Culpan et al. \(2021\)](#). It is not surprising that a sample extending to 500 pc above and below the Galactic plane may include a significant fraction of kinematically heated sources, suggesting older thick-disk or halo population stars. Two of the four stars with tangential velocities exceeding 200 km/s, Feige 46 and LSIV –14 116, confirmed as halo stars ([Dorsch et al. 2020](#)), exhibit no RV variability. SB744 is also identified as a halo star with no RV variability ([Németh et al. 2021](#)). While it is unclear whether TYC144-2049-1 is a MS or BHB star, its measured RV of  $211 \pm 6$  km/s, suggests it is probably a member of the halo population. These stars are not excluded in the scale height and space density calculations as it has marginal impact on the results. Obtaining reliable systemic velocities of all members of this sample for a kinematic analysis is the ambition of a future paper.

## 5. Content of the catalogue

In this section we detail the content of the 500 pc sample in terms of the variety of astrophysical objects found in the *Gaia* CMD

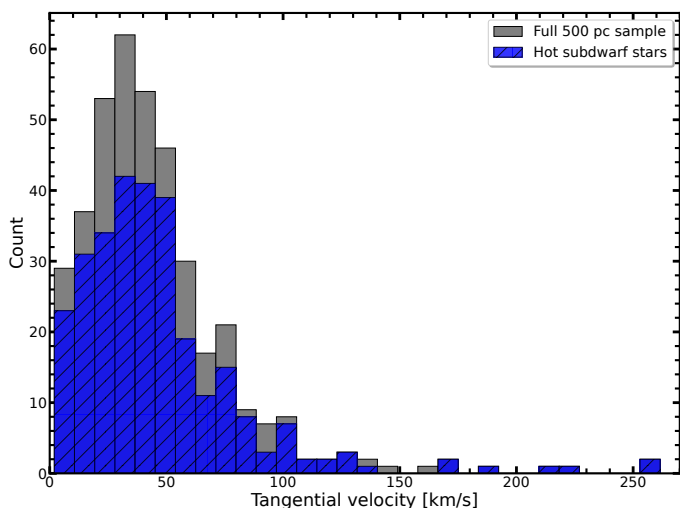


Fig. 10: Histogram displaying the tangential velocity of the full 500 pc sample (grey) and the confirmed hot subdwarf stars (blue) calculated using *Gaia*'s proper motion measurements.

parameter space as illustrated in Fig. 11, which is accompanied by table 3.

Spectroscopic class	Number	Fraction
Hot Subdwarfs (table A.1)	305	77%
sdB	178	$58.4^{+2.9}_{-2.8}\%$
sdOB	65	$21.3^{+2.2}_{-2.5}\%$
sdO	32	$10.5^{+1.5}_{-2.0}\%$
He-sdB/OB/O	30	$9.8^{+1.5}_{-2.0}\%$
sdO/B+MS (table A.2)	48	$15.7^{+1.9}_{-2.3}\%$
Other constituents (table A.3)	92	23%
CV	41	$44.6^{+5.0}_{-5.2}\%$
WD	11	$12.0^{+2.6}_{-4.2}\%$
WD+MS	3	$3.3^{+1.0}_{-3.0}\%$
sdA	4	$4.3^{+1.3}_{-3.2}\%$
MS/BHB	26	$28.3^{+4.2}_{-5.1}\%$
Removed	7	$7.6^{+1.9}_{-3.7}\%$
<b>Overall total</b>	<b>397</b>	<b>100%</b>

Table 3: Catalogue classification.

### 5.1. Hot subdwarf stars

The sample is primarily made up of hot subdwarf stars (77%) which are listed in table A.1 and table A.2 for the non-composites and composites, respectively, and reports 83 new discoveries. Most previous dedicated surveys of hot subluminous stars have avoided the crowded and dusty regions of the Galactic mid-plane and were thus restricted to high Galactic latitudes (Vennes et al. 2011). It comes as no surprise then that most of the newly discovered hot subdwarfs in this programme are concentrated in the disk. This is best illustrated in Fig. 12, where a clear deficit of objects near the Galactic plane is seen in the previous

catalogue of known hot subdwarf stars. The number of missing non-composite hot subdwarf stars due to interstellar extinction in this 500 pc selection is expected to be minimal (see Sect. 6 for an estimate of the completeness). This work builds upon previous studies and finds the majority of new objects below  $b \approx 30$  degrees. We further report that 12 of the new systems show an infrared excess in their spectral energy distributions (Sect. 5.3) revealing them as possible composite-colour binaries. Four systems that were previously known, but were thought to be single hot subdwarfs, also show an infrared excess and are newly identified composite-colour binaries. HD 76431 is known to be a post-HB star (Khalack et al. 2014) which appears to be evolving through our selected parameter space and is positioned above the hot subdwarf cloud in the CMD (see Fig. 11, where HD 76431 is the only sdB with  $G < 2$ ). With a spectrum resembling an sdB, it will be counted as such in this work.

Compared to the most recent previous catalogues of hot subdwarf stars (specifically Geier et al. 2017; Geier 2020; Culpan et al. 2022), we find the fractions of non-composite sdB and sdOB stars ( $50.2^{+2.9}_{-2.2}\%$  and  $16.7^{+1.9}_{-2.4}\%$ , respectively) to be somewhat different, yet the total number of sdB + sdOB stars is exactly the same ( $\sim 67\%$ ); this is probably due to the use of low-dispersion (published) spectra, where the weak He II 4686 Å line, which would differentiate between sdB and sdOB, might be present but undetected.

### 5.2. Known hot subdwarf stars in close binaries

Dedicated radial velocity variability (RVV) searches have indicated that at least one-third of hot subdwarfs reside in a close binary system with either a compact companion such as a WD, or a cool MS (dM) or brown dwarf (BD) (Maxted et al. 2001; Morales-Rueda et al. 2003; Napiwotzki et al. 2004; Copperwheat et al. 2011; Kawka et al. 2015; Kupfer et al. 2015; Geier et al. 2015, 2022). Currently, there are over 300 systems that host companions which are too faint to contribute any detectable flux to the observed light, yet are revealed by the Doppler shifts they induce in the spectral lines of the far brighter hot subdwarf. Additionally, they may also be revealed by the photometric variability they bring about in their light curves (e.g. Schaffenroth et al. 2019). Schaffenroth et al. (2022, 2023) carried out the most recent investigation on the nature of the close companions to hot subdwarf stars of type B (sdB) using data from the Transiting Exoplanet Survey Satellite (TESS) and the K2 space mission. Combining all the observational efforts listed above, a total of 36 systems, which either host WD, dM, or BD companions, are members of our 500 pc sample. This gives a close binary fraction of  $12.3^{+1.7}_{-2.2}\%$  assuming a binomial distribution and without taking inclination into account. This fraction is probably a lower limit due to the 83 newly discovered systems which are yet to be investigated for signatures of binarity. This fraction has no impact on the analysis performed in this work as outlined in Sect. 4 as the close binary population is assumed to be complete (see Sect. 6). As such, an estimate of the fraction of this complete population could be directly used to constrain formation channels. An analysis of these systems, which will be the focus of a future paper, is vital for resolving the poorly understood short-lived phase of common-envelope evolution.

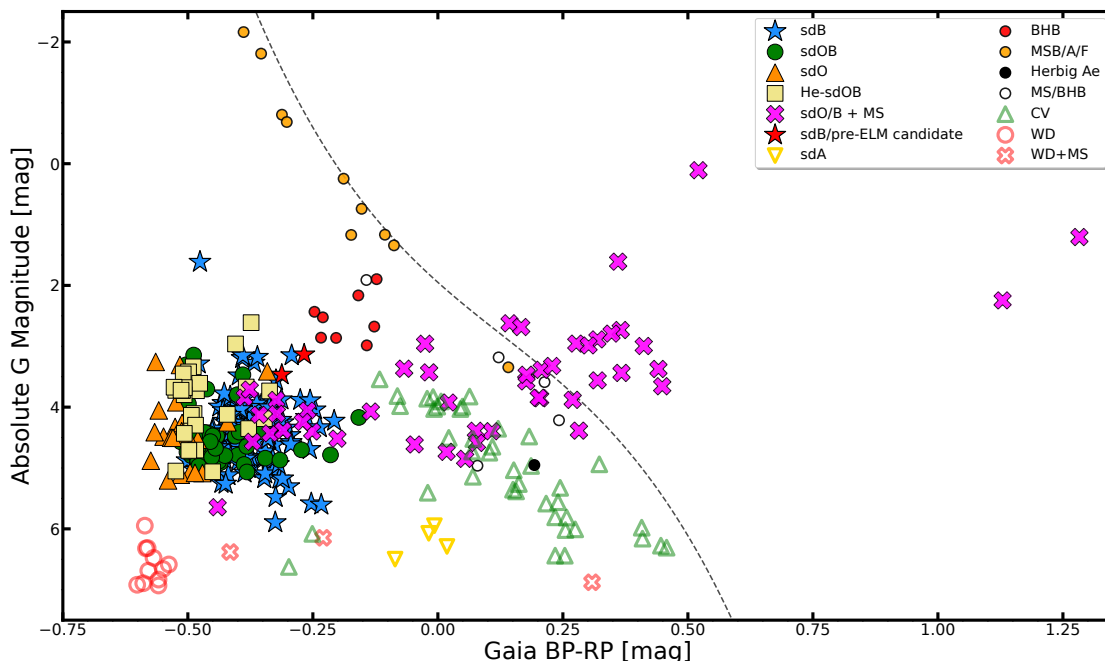


Fig. 11: Colour-magnitude diagram of all 397 members with clean astrometry (Sect. 2.2) in the 500 pc sample and colour-coded accordingly. Confirmed sources have been corrected for the effects of reddening (Sect. 6).

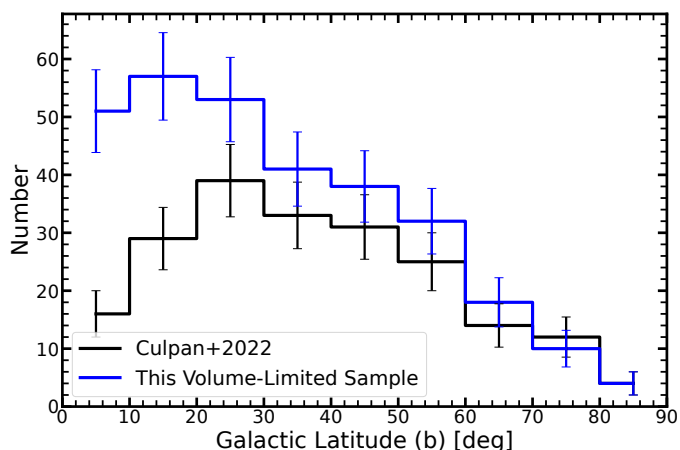


Fig. 12: Number distribution of the hot subdwarf stars in our volume-limited sample as a function of Galactic latitude, divided into nine bins of  $|b|$ . Black represents the catalogue of Geier (2020)/CG22 within 500 pc, whereas blue are those stars in this volume-limited edition. The error bars reflect statistical Poisson errors.

### 5.3. Hot subdwarf stars with cool main sequence companions

At least one-quarter of all hot subdwarfs are observed to host F/G/K-type MS companions (Girven et al. 2012; Solano et al. 2022) which are bright enough to be seen in the combined light of the system. However, the necessary cleaning during the construction of the catalogue of CG22 came at the expense of the exclusion of several known systems, in particular those hot subdwarfs located redwards of the empirical MS rejection criterion in the *Gaia* CMD. To date, there are 26 known sd+F/G/K sys-

tems with solved orbital parameters (Vos et al. 2012, 2013, 2017, 2019; Barlow et al. 2013; Otani et al. 2018; Deca et al. 2018; Molina et al. 2022; Otani et al. 2022). The study of such systems is crucial for constraining parameters of the stable RLOF channel (Vos et al. 2018; Molina et al. 2022) by which they are formed. It is essential to identify these systems as the population is known to be incomplete, and would otherwise bias the analysis of this paper. These companions are of MS types F, G, or K, which may dominate the optical spectral range and shift the systems CMD position into the MS. At least 18 such systems within 500 pc exist, including nine solved long-period systems, and are included in this catalogue. All manually added sources are indicated in table A.2 with an asterisk which mainly comprises those previously known composite binaries located within the MS, barring a single source that failed the `phot_bp_rp_excess_factor_corrected` criterion in CG22 (EC05053-2806), which probably stems from the bright F-type companion to the hot subdwarf. Many of these manually added systems host brighter companions of type F which we expect to be the least complete population.

To estimate the total number of composite systems we constructed spectral energy distributions (SEDs) for all candidates regardless of their RUWE values. These SEDs were used to identify hot subdwarf stars that exhibit atypically red infra-red (IR) colours, which can be attributed to the presence of a cool unresolved companion. Examples of a single and composite SEDs are shown in Fig. 13: K-type companions are detectable by their contribution in the IR, G-types contribute optical and dominate in the IR, and F-types tend to dominate in the optical as well; all of these companions are well detected by SEDs. In particular the K-type companions are well detectable in the SED, even if they are difficult to see in spectral optical data. Hotter (O/B/A) companions outshine the hot subdwarf at (almost) all wavelengths, whereas cooler companions (late M-type) contribute too little to be detectable even in the IR.

We used the SED fitting method described by Heber et al. (2018) to identify composite colour binaries and constrain the nature of the cool companions.<sup>10</sup> To model the two stellar components in the SED, we made use of two model grids. The hot components were modelled using our standard grid computed with ATLAS12 (Kurucz 1996; Irrgang et al. 2018), which covers the full hot subdwarf parameter space and has been used extensively for many analyses of sdB stars, for example by Schafferoth et al. (2022). For the MS component, a grid of synthetic PHOENIX stellar atmosphere models was used (Husser et al. 2013) which can be downloaded from the Göttingen Spectral Library.<sup>11</sup> The best fit to the observed SED was achieved using  $\chi^2$  minimisation. Free fit parameters were the angular diameter ( $\theta$ ) of the hot subdwarf, the effective temperature of both components, the surface ratio  $R_{\text{cool}}^2/R_{\text{hot}}^2$ , as well as the interstellar reddening parameterised by the colour excess  $E(44-55)$ . Here, we used the reddening law of Fitzpatrick et al. (2019). Because the surface gravity and metallicity of both components cannot be determined from the SED, we had to fix these values. The companion's surface gravity was fixed to 4.3, a reasonable value for possibly evolved MS companions. Their metallicity was fixed to solar. In the case of the hot subdwarf, the metal abundances were fixed to average sdB values from Pereira (2011) and the surface gravity was constrained to spectroscopic values where possible.

Of the spectroscopically identified hot subdwarfs in the sample, including those manually added systems, 48 (16%) are composite-colour binary systems (see Fig. 13 for several example fits). The majority are cooler G-, and K-type companions. Furthermore, we use the derived temperature of the companion and interpolate between table 15.7 given in Cox (2000), to discern its spectral class. A total of 16 systems have been newly identified, including 5 that were previously categorised as single hot subdwarfs. This fraction is somewhat lower than has previously been found. Work done by Stark & Wade (2003) identified composite-colour hot subdwarf binaries by means of colour-colour diagrams including IR fluxes from 2MASS and arrived at an estimate of 30% after approximating a volume-limited sample. The works of Thejll et al. (1995), Ulla & Thejll (1998), and Girven et al. (2012) all contributed to the current list of composite-colour hot subdwarf star binaries identified using colour-colour diagrams. Schafferoth (2016) systematically constructed SEDs of hot subdwarf stars of various different natures from 5 different samples, arrived at the same estimate of 30%. These fractions are corroborated by the most recent study by Solano et al. (2022) who estimated 25%. Our lower estimate is likely due to the MS rejection criterion. Although several systems located within the MS were added manually, there remains a strong observational bias against detecting these systems as they are currently mainly discovered through UV excess rather than infrared excess or spectroscopic observation (Kawka et al. 2015) owing to the similar spectral coverage and large luminosity difference of the companion to that of the hot subdwarf. The impact of these missing systems will be discussed in Sect. 6 when assessing the completeness of the sample.

Lastly, the SEDs for those sources that failed our RUWE < 7 quality cut were inspected to search for potentially genuine composite hot subdwarf binaries, as well as potentially removed single sources. Barring GALEXJ110733.7-454424, a newly discovered composite sdB+G/K that was excluded from the sample due to a poor astrometric solution (see Sect. 2.2), all sources with RUWE > 7 are consistent with single MS stars. Among these, 21

have spectra in the LAMOST DR8 archive and exhibit the spectral features characteristic of MS A-type stars.

By combining the SED method with the *Gaia* parallax measurements and a spectroscopic analysis it would also be possible to derive radii, masses, and luminosities. Such an analysis will be performed in a follow-up paper once the spectroscopic analysis is complete. The same routine as described above is used in Sect. 6.2 to generate mock SED fits in our attempt to estimate the number of missing composite-colour hot subdwarfs in our sample.

#### 5.4. Cataclysmic variables

Barring the hot subdwarf population, the CVs are the next most numerous objects in our selection with a count of 41 (10%), which includes three newly discovered systems: Gaia DR3 5389717630410364160, PB5919, and TYC7791-1293-1. Their presence in the sample stems from the fact that they photometrically fall in close proximity to the hot subdwarfs in the HRD, with a maximum density in the region  $G_{\text{BP}} - G_{\text{RP}} \approx 0.56$  and  $G_{\text{abs}} \approx 10.5$  (Abril et al. 2020). Moreover, the subtypes of intermediate polars (IPs) and nova-likes concentrate close to  $G_{\text{BP}} - G_{\text{RP}} \approx 0.37$  and  $G_{\text{abs}} \approx 5.63$  due to these stars being optically dominated by their bright accretion disks. Recently, Pala et al. (2020) compiled a volume-limited sample of CVs which constituted a total of 42 members within 150 pc. Since our sample is optimised for the selection of hot subdwarf stars, only two of the CVs listed in (Pala et al. 2020) are in our sample: IX Vel and CD-42 14462, both indeed Nova like systems which demonstrate strong hydrogen emission lines, indicative of a bright accretion disk. Given the parameter space our selection encapsulates in the HRD, the presence of these systems in our sample is consistent with what is expected (Abril et al. 2020). The remaining 39 systems are primarily too faint to meet our absolute magnitude selection, or are otherwise located within the MS.

#### 5.5. WDs, post-AGBs, and CSPNe

A small fraction of stars in our sample are hot and bright WDs at the beginning of their cooling track. In the bottom left corner of Fig. 11 a clustering of WDs can be seen below the hot subdwarf cloud. As they are bright, all are well known barring two newly discovered and analysed systems in Reindl et al. (2023) - J17514575+3820157 and J194511.31-445954.57. GD 1532, currently listed as a known sdB in the SIMBAD Astronomical Database (Wenger et al. 2000), has been reclassified as a WD in this work. The population of WDs in our sample also includes some identified CSPNe which can be found in both the Hong Kong/AAO/Strasbourg  $H\alpha$  (HASH) PN catalogue (Parker et al. 2016) and that of Chornay & Walton (2021), such as NGC 7293 and M27 which host DAO WDs in their cores (Gianninas et al. 2011). Several of these post-AGBs and CSPNe, however, have bright and luminous sdO cores, such as PNA6636, NGC 1360, NGC 1514, and MWP 1 (Greenstein & Minkowski 1964; Mendez & Niemelä 1977; Feibelman 1997). To be in line with the nature of this work's classification scheme as outlined in Sect. 3.3, those identified CSPNe or post-AGBs with spectroscopically classified sdO cores, are counted among the sdO stars for the analysis and statistics of our sample. Those CSPNe, as well as the PG 1159 stars with identified WD cores, will be counted among the spectroscopically identified WDs. KPD0005+5106, however, for example, is a known pre-WD object (Werner & Rauch 2015) with O(He) spectral type whose origin is still de-

<sup>10</sup> This SED fitting routine was initially developed by Andreas Irrgang.

<sup>11</sup> <http://phoenix.astro.physik.uni-goettingen.de/>

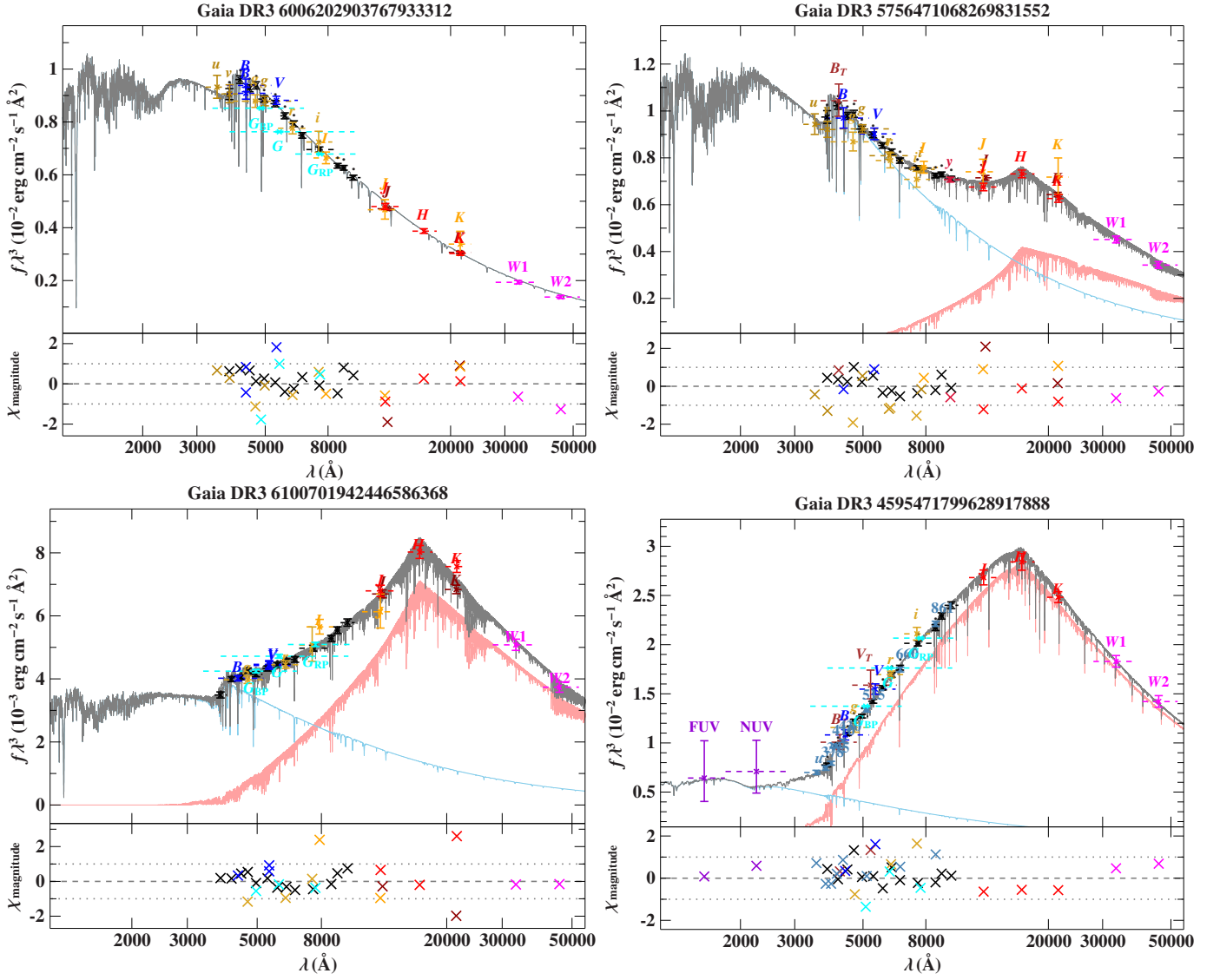


Fig. 13: Example spectral energy distribution fits for a single sdOB (top left), an sdB+M0 (top right), sdB+G9V (lower left), and a sdB+F6V (lower right). Photometric fluxes are shown as coloured data points with their respective filter widths as dashed horizontal lines. The grey line shows the combined model spectrum, while the individual contributions of the hot subdwarf and MS companion are given by the blue and red lines, respectively. The different photometric systems in these plots are assigned the following colours: JPLUS (steel blue; von Martens et al. 2024), Gaia XP (black; Gaia Collaboration 2022), Gaia G/BP/RP (cyan; Gaia Collaboration 2022), WISE (magenta; Cutri et al. 2021), SkyMapper (dark gold; Onken et al. 2019), SDSS (gold; Alam et al. 2015), GALEX (dark violet; Bianchi et al. 2017), Pan-STARRS (crimson; Chambers et al. 2016), VISTA (maroon; Cioni et al. 2011; McMahon et al. 2013), DENIS (orange; DENIS Consortium 2005), 2MASS (red; Cutri et al. 2003), Johnson (blue; Henden et al. 2016; Girard et al. 2011) and Tycho (brown; Høg et al. 2000). Citations for all photometric data used in this work can be found in the acknowledgements.

bated. It will be counted among the helium sdOs in this work. On this note, it is important to emphasise that many bright sdO stars share the same properties of several CSPNe (e.g. Gianninas et al. 2010) despite having very different evolutionary histories. Including this population in future monitoring programmes in the context of volume-complete samples of hot subluminous stars will certainly be of interest to help better disentangle the outcomes of both single and binary stellar evolution theory.

### 5.6. Other objects of diverse and ambiguous classifications

There are 30 (10%) stars identified in this sample as late B- or early A-type stars, indicating that they are considerably cooler than sdB/O stars. They are probably either main sequence, blue horizontal branch stars, or show sdA-type spectra, which are characteristic of many different evolutionary classes (Pelisoli et al. 2017). Although most BHBs would be situated below the main sequence in the CMD, confirming this classification is difficult with the majority of the obtained spectra being low resolution. However, we couple a preliminary analysis of these spectra to constrain the effective temperature and surface gravity with

our SED fitting routine (Sect. 5.3) to obtain the stellar radii and masses of these stars. We find ten to be consistent with MS stars; they are indicated accordingly in Fig. 11. Another eight have radii between 0.5 and 1.0  $R_{\odot}$ , respectively, making MS an unlikely evolutionary class for these stars. Identifying them as probable BHB candidates, all of these objects are situated in close proximity to the blue horizontal branch in the CMD of Fig. 11 between the hot subdwarf cloud and the MS. Five stars have RUWE values greater than 4, which we deem to be an unreliable astrometric solution and are classed as MS/BHB. One source in our sample is a known Herbig Ae star: UY Ori A (Fairlamb et al. 2015).

[PS72]97, Gaia DR3 2513538251735261696, Gaia DR3 4318061098980872960, and Gaia DR3 6058834949182961536 are four objects in our sample that demonstrate MS A-type-like spectra, but have absorption lines that are too broad to be classified as a MS star. It is probable that these systems are helium-core white dwarf progenitors passing through our parameter space towards the WD cooling track and indeed [PS72]97 and Gaia DR3 2513538251735261696 have recently been identified as such (Kosakowski et al. 2023). Their positions in the CMD indicated as gold triangles in Fig. 11 are clearly grouped into a specific parameter range which is well separated from the hot subdwarf stars. These objects are accordingly classed as sdAs in this paper and will be subject to a more detailed spectroscopic analysis to disentangle their evolutionary origin in the future.

Lastly, two systems, TYC3135-86-1 and HD337604, have spectra resembling B-type MS stars. These stars have effective temperatures close to 20,000 K, but radii of  $0.35 \pm 0.02$  and  $0.42 \pm 0.02 R_{\odot}$ , respectively. This places them above the cool end of the EHB and below the MS. We class these two cases as pre-ELM/sdB candidates and indicate them as red stars in Fig. 11. These stars require follow-up observations to discern their true natures.

## 6. Completeness of the 500 pc sample

A completeness estimate is an essential property for any sample of stars that aims to test physical theories about stellar evolution. While we have demonstrated statistical homogeneity when accounting for the scale height, this alone cannot serve as a completeness estimate. The non-negligible influence of the Galactic disk structure at the 1 kpc scale, which corresponds to the diameter of our sample, necessitates a qualitative exploration of completeness in this section.

### 6.1. Reddening by interstellar extinction

The completeness of CG22, the source of this sample, is estimated to be 80 – 90% for single sources and unresolved binaries overall, with near completeness up to 1.8 kpc above and below the Galactic plane. However, within the Galactic plane, interstellar extinction-induced reddening can shift a source to redder colours, potentially moving it out of our selected region in the CMD. To account for this, we obtained reddening estimates of the form  $E(44-55)$  for all non-composite hot subdwarfs using a 2D line-of-sight SED fitting routine, as detailed in Sect. 5.3. Where available, literature parameters of  $T_{\text{eff}}$ ,  $\log(g)$  and  $\log(y)$  were used to constrain the fit, where  $T_{\text{eff}}$  was otherwise left as a free parameter and  $\log(g)$  and  $\log(y)$  were fixed to typical atmospheric hot subdwarf parameters. For the composite-colour hot subdwarfs, however, we use the reddening given by the 3D

Stilism<sup>12</sup> (Lallement et al. 2014; Capitanio et al. 2017) reddening maps because atmospheric parameters for these sources were often unavailable. Without precise atmospheric parameters of all targets to constrain the SED fitting procedure, the  $E(44-55)$  parameter can become unreliable due to a degeneracy between temperature and extinction.

The lower panel of Fig. 14 presents a CMD illustrating the shift each hot subdwarf undergoes when reddening is considered. Blue stars represent non-composites corrected for  $E(44-55)$ , while magenta stars depict composites corrected using Stilism. The impact of this correction is indicated by black-dotted lines, illustrating the shift in each source in this parameter space. The upper panel provides a colour-scaled skyplot, revealing the directional dependency of reddening, with the largest values concentrated towards the Galactic centre, as expected.

In the CMD parameter space, a typical non-composite hot subdwarf would require a reddening of  $\approx 0.6$  mag to fall outside our selection. The average reddening towards the Galactic centre (covering about 17% of the sky with  $|b| < 30^{\circ}$  and  $300^{\circ} < l < 60^{\circ}$ ) for our targets in the 500 pc sample, according to Stilism reddening maps, is  $\approx 0.11$  mag. We argue that reddening has a negligible impact on the completeness of the single sources and unresolved binaries, and the sample should be essentially complete up to 500 pc across the sky. An exception is UCAC4 436-075435, an sdOB with a calculated reddening of  $E(44-55) = 0.605$  mag. While this system initially appears in the bottom right corner of the CMD in Fig. 14, it aligns with the centre of the hot subdwarf cloud once reddening is corrected. As no other non-composite hot subdwarf in our sample exceeds a reddening of 0.3 mag, we anticipate that reddening does not significantly affect the completeness of our sample.

It is important to note that the population of low-mass hot subdwarf stars or helium-core WD progenitors such as HD 188112 typically occupy a region closer to the MS and are probably highly incomplete in our sample. Given their low occurrence rate in our selected parameter space, we do not account for them here and assume completeness for all single sources and hot subdwarf binaries which host companions that have little impact on the overall colour of the system, such as WD or cool MS or BD companions. However, incompleteness due to extinction will become an increasing issue for future volume-limited samples that extend beyond 500 pc.

The situation is different for the composite binary hot subdwarfs, where the MS companion inherently shifts the system to redder colours in the *Gaia* CMD parameter space, irrespective of interstellar extinction. Assuming clean astrometry, the companion's presence increases the overall brightness of the system, shifting its position in the CMD upwards instead of downwards. This creates a trend of increasing absolute magnitude with increasing colour index. The extent of this shift is not straightforward. In the simplest case, the shift is proportional to the spectral type of the MS companion, with earlier types being brighter than later types, and their brightness exponentially more impactful than their colour. However, the exact evolutionary status of both the hot subdwarf and MS is unknown, and the relative contribution of each to the system's flux is uncertain, influencing the system's CMD position.

### 6.2. The missing composite-colour hot subdwarfs

To estimate the completeness of our sample and identify potential missing composite systems, we employed a theoretical

<sup>12</sup> <https://stilism.obspm.fr/>

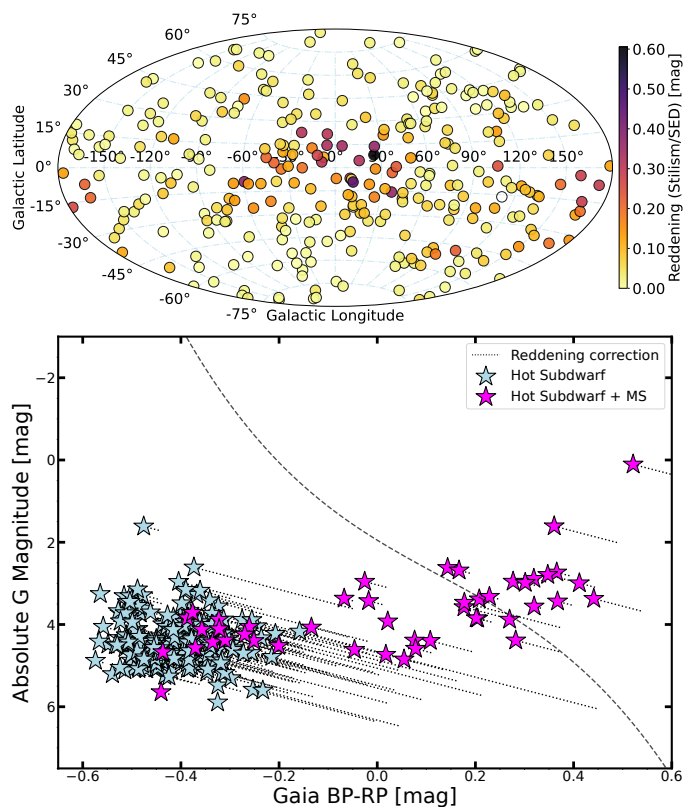


Fig. 14: Plot to illustrate the effect of interstellar extinction on the 500 pc sample. Top: Skyplot of the 500 pc sample which is colour-coded according to the reddening parameters given by both Stilism and the SED fits. Bottom:  $G_{BP}-G_{RP}$  vs  $M_G$  diagram of the same sources where blue stars indicate non-composite hot subdwarfs that have been corrected for interstellar extinction using the E(44-55) SED estimates, and magenta stars indicating composite-colour hot subdwarfs that have been corrected for using Stilism. The correction shift is shown with the black dotted lines. Systems hosting subgiant companions have been excluded from the plot.

cal approach. Mock binary SEDs were generated, and resulting colours and absolute magnitudes were computed for various combinations of component parameters. MS companion masses ranged from  $0.25 M_{\odot}$  to  $3.0 M_{\odot}$  at  $0.05 M_{\odot}$  intervals, considering three types of hot subdwarfs: sdB, sdOB, and He-sdO. Typical atmospheric parameters were assumed for each type of hot subdwarf based on our sample. Companion parameters were calculated from their intermediate age, defined as the point where central hydrogen abundance reaches 30% with a threshold for effective temperatures below 11,000 K (see Heber et al. 2018, for the fitting routine details). Figure 15 displays the results of these calculations, showing good agreement with the identified composites in our sample. An exception is NGC 1514 in the upper right corner, hosting a spectral type A0 horizontal-branch star companion at the centre of a planetary nebula. BD-03 5357 and HD 185510, hosting subgiant companions, are not included in this plot due to plot limits. Companion masses of 1.1, 1.0 and 1.0 for the He-sdO’s, sdB’s, and sdOB’s, respectively, lie closest to the MS rejection criterion. Accounting for the effects of reddening due to interstellar extinction with the average Stilism value near the Galactic centre for our sources ( $\approx 0.11$  mag), the detectable companion masses are decreased by  $\approx 0.1 M_{\odot}$  each.

Corrected for the relative abundances of each hot subdwarf class in our sample, this yields an average companion mass of  $0.91 M_{\odot}$  - the theoretical maximum observable mass in our selection. Consequently, our sample is expected to be, on average, complete for companions of spectral type G5 or later across the entire sky. This estimate is supported by the fact that all manually added systems in our sample host companions of spectral types G or earlier. However, it remains challenging to estimate the number of missing composites without assuming an underlying mass distribution for the MS companions.

Stark & Wade (2003), approximating a volume-limited sample, derived a composite-colour hot subdwarf fraction of 30%, while a more recent study by Solano et al. (2022) arrived at 25%. Taking the average of these two studies, our initially observed fraction of 16% (48 systems) can then be adjusted to 27.5%, suggesting that  $\approx 31$  systems may be missing from our selection. This estimate probably represents a lower limit, considering biases against composite-colour binaries in previous samples of known hot subdwarf stars. Consequently, we infer a 90% overall completeness for the hot subdwarf star constituents, assuming a homogeneous distribution of composite-colour hot subdwarfs. To account for these estimated missing systems, we add the relative error of the 31 systems to the upper uncertainty on the derived mid-plane density, resulting in  $\rho_0 = 6.15^{+1.16}_{-0.53} \times 10^{-7}$  stars/pc<sup>3</sup>.

We now take an observational standpoint to predict the number of missing composites in our selection by cross-matching a *Gaia* database query with GALEX. Hot subdwarfs in unresolved binary systems with an F or G-type MS counterpart should show an excess in the ultraviolet (UV) (see Downes 1986, for early works). The selection criterion for the executed query to the *Gaia* database, and the defined UV excess for sources with GALEX detections are given in table 4.

1. Selection criterion for the queried region shown in Fig. 15.
$G_{abs} < 17.7(G_{BP} - G_{RP})^3 - 6.9(G_{BP} - G_{RP})^2 + 7.35(G_{BP} - G_{RP}) + 1.95$
$< 7 - 3(G_{BP} - G_{RP})$
$> 7(G_{BP} - G_{RP}) - 3.8$
$> -1$
$RUWE < 7$
$parallax\_over\_error > 5$
2. UV excess criterion for queried sources with GALEX data.
$FUVmag - NUVmag > 2.5 - 1.5(NUVmag - Gmag)$

Table 4: Selection criteria.

The queried area, encompassed by the black dashed lines in Fig. 15, accounts for a reddening of up to 0.3 magnitudes as well as the full range of masses of the companions to hot subdwarfs which were calculated from our mock SEDs. The query does not cover the parameter space occupied by the hot subdwarfs hosting subgiant companions such as BD-03 5357 and HD185510. This query yielded 1,003,196 sources, with 516,902 having GALEX detections (51.5%). Among these, 31 exhibit UV excess as depicted in Fig. 16, and within this subset, 21 are unidentified candidates. Based on the number of selected sources in GALEX compared to *Gaia* - 51.5% - that would suggest that  $\approx 42$  candidate systems are within the MS given our selection criteria. This number is in reasonable agreement with our estimate given above, especially if we account for a number of WDs hosting MS companions which would be indistinguishable using this method. Spectroscopic follow-up and RV monitoring of



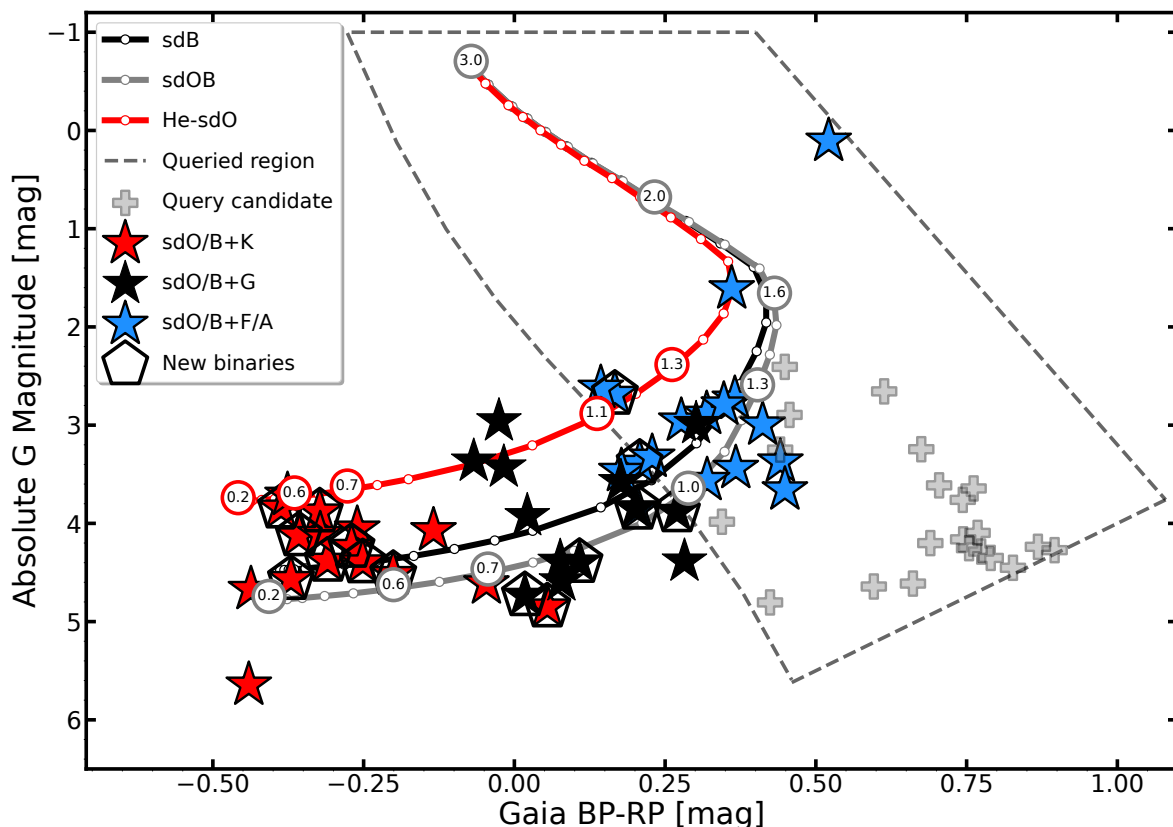


Fig. 15: CMD displaying the results of the mock SED fits for different combinations of hot subdwarf (sdB-black; sdOB-grey; He-sdO-red) with MS companions. Each circle along the tracks indicates a  $0.05 M_{\odot}$  step in the companion mass between  $0.2 M_{\odot}$  and  $3.0 M_{\odot}$  where several have been labelled as reference points. These tracks indicate that a companion mass of  $1.0 - 1.1 M_{\odot}$  is the maximum expected to be detected in this sample. The calculations do not account for reddening and can be compared to the reddening-corrected hot subdwarf composite systems given in the plot. These composites have been divided up into companion types to emphasise that the sample is expected to be complete for all K-type companions. Newly discovered systems are indicated with an additional encompassing pentagon. BD-03 5357 and HD185510 are outside the plot limits; they are known to host subgiant companions. Queried candidates that will be followed-up in a spectroscopic monitoring campaign are shown as grey plus signs.

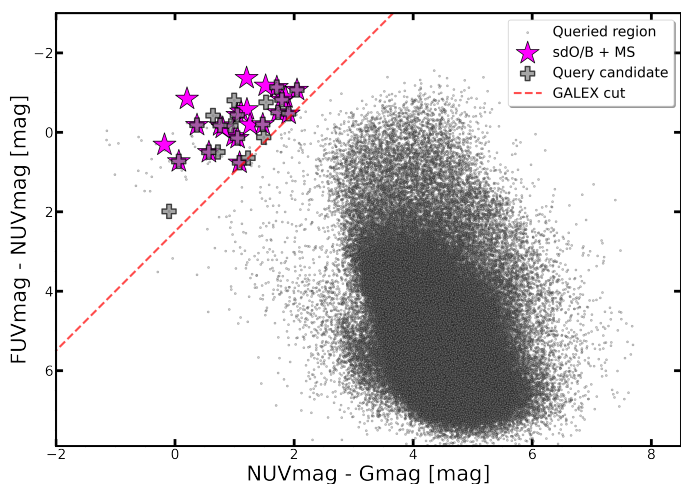


Fig. 16: Colour-colour diagram displaying the 516,902 queried sources with GALEX detections. The red dashed line delineates our UV-excess cut, and to its left are situated all known composite hot subdwarfs (magenta stars) within 500 pc. The 21 promising composite candidates are represented by grey plus signs.

these candidates are needed in order to pursue this missing population.

### 6.3. Hot subdwarfs as companions to Be stars

Be stars are rapidly rotating B-type stars, either MS or evolved, which have shown some form of emission lines at some point during their lives (Porter & Rivinius 2003). Recent observational evidence has supported the formation of early-type Be stars to be rooted in binary interaction (Bodensteiner et al. 2020), where the rapid rotation and decretion disk is a result of a previous episode of mass transfer from a nearby companion. If this were true, then many Be stars should host the remnants of the donor star. Indeed, several evolved compact companions to Be stars are known, including a handful of stripped helium burning hot subdwarf stars which are predicted to make up the majority of the companions (Pols et al. 1991). Due to their much higher intrinsic luminosity ( $\approx 100$  times) and similar spectral energy range, Be stars can effectively hide a companion hot subdwarf in the optical sector. Ultraviolet (UV) data is required to distinguish these components which has been the method of detection of most previous studies. More recently, El-Badry et al. (2022) performed a dedicated search for bloated stripped companions to Be stars using data from the APOGEE survey. From a well-defined parent sam-

ple of 297 Be stars, one mass-transfer binary was identified, and predicted to eventually evolve into a Be + sdO binary system. Because the timescale of this mass transfer phase is predicted to be fleeting ( $\approx 1$  Myr), the authors estimate that (10 – 60)% of Be stars host stripped companions. The BeSS database offers an up to date count of all the known Be stars, as well as offering high-quality spectra for most sources. By querying the archive, we find 305 Be stars within 500 pc. Following the prescription of [El-Badry et al. \(2022\)](#), this would imply that there are 28 – 170 hot subdwarf stars hiding behind classical Be stars in our 500 pc sample.

Analysing a sample of 13 Be stars using Hubble Space Telescope/STIS far-ultraviolet spectra, [Wang et al. \(2021\)](#) identified the presence of a hot sdO companion in ten of these stars. Notably, seven of these companions are located within 500 pc. These systems are exceedingly difficult to detect, especially since even the brightest sdO companions may only contribute  $\approx 1\%$  of the total flux ratio ([Peters et al. 2016](#)). Hot subdwarfs around Be stars have probably been formed by stripping through binary interactions, but tend to possess larger masses and radii than the general population discussed in this work. This stems from an entirely different evolutionary channel for binary stars of high mass. To this end, we refrain from including them in the analysis presented in this work, and leave it as an open question for future studies as to how they may be integrated into the population of known hot subdwarf stars.

## 7. The birthrate of hot subdwarf stars

In Sect. 4, we determined the mid-plane density of the non-composite hot subdwarf stars in our sample to be  $\rho_0 = 5.17 \pm 0.33 \times 10^{-7}$  stars/pc<sup>3</sup>, which increases to  $\rho_0 = 6.15^{+1.16}_{-0.53} \times 10^{-7}$  stars/pc<sup>3</sup> when considering the known composite-colour hot subdwarfs within 500 pc and accounting for incompleteness (see Sect. 6).

To estimate the birthrate, we rely on theoretical evolutionary lifetimes from [Han et al. \(2003\)](#). Interpolating between their  $0.5M_{\odot}$  and  $0.45M_{\odot}$  models, we derive a value of  $\tau = 1.98 \times 10^8$  years, adjusted with a 10% increase to include the helium shell burning phase. Employing a Monte Carlo approach, assuming an error of 50 Myr on the hot subdwarf lifetime, our calculated median birthrate is  $\rho_0/\tau = 3.35^{+1.24}_{-0.77} \times 10^{-15}$  stars/pc<sup>3</sup>/yr<sup>-1</sup> for our sample. Assuming a Galactic volume of  $5 \times 10^{11}$  pc<sup>3</sup> ([Zombeck 1990](#)), [Han et al. \(2003\)](#) give a prediction of  $10 \times 10^{-14}$  stars/pc<sup>3</sup>/yr<sup>-1</sup> for their best-fit model, which is  $\sim 30$  times higher than our observational estimate, even after accounting for our attempt to correct for the incompleteness of composite binaries. The theoretical estimate halves when this same selection effect is accounted for in the models, although is still on the same order of discrepancy as stated above when composites are excluded from our sample. The precise fraction of composites among all hot subdwarfs would be a very decisive number to distinguish simulation sets (see Table 2 of [Han et al. 2003](#)). Unfortunately it is difficult to measure this fraction as discussed throughout this paper.

While these estimates may appear conflicting, it is essential to note that they might represent slightly different quantities. This work provides a comprehensive count of all hot subdwarfs within this parameter space, without distinguishing, for instance, the pure horizontal branch (HB) evolution considered by [Han et al. \(2002, 2003\)](#). Our sample, representing the general local population of hot subdwarf stars in the solar neighbourhood, differs from the approach taken by [Han et al. \(2003\)](#),

whose birthrate calculations apply to the entire Galactic population. Notably, our local volume-limited sample under-represents the thick-disk population mentioned by [Han et al. \(2003\)](#), where a higher birthrate is predicted compared to population I stars under similar parameters. Despite potential overestimations in our sample completeness, the significant discrepancy remains challenging to explain, particularly given our density estimate focusing on the mid-plane, where the highest concentration of stars is expected. Further characterisation of this sample may give clues about the underlying reason for this miss-match. For instance, refinement of the BPS models may be sought by observationally constraining the relative number of systems with MS and WD companions, which would help to constrain model input parameters and thus shed insight on the relative importance of each of the formation channels. This ambition, will be the main focus of a future paper.

## 8. Summary

The creation of this all-sky volume-limited sample, defined using the accurate parallax measurements from *Gaia*'s DR3, is the first of its kind. It has contributed to the identification and classification of 83 new hot subdwarfs, adding to a total of 305 well-classified or otherwise updated hot subdwarf systems within 500 pc. Among these, 48 systems (16%) exhibit infrared excess in their SED fits, and they have been categorised as composite systems hosting MS companions. Notably, 16 of these composites are newly identified in this study, primarily comprising systems with K- or G-type companions, which are more challenging to detect through optical spectroscopy compared to companions of type F, dominating the optical data. Additionally, the sample revealed three nova-like CVs closely situated to the hot subdwarfs in the *Gaia* colour-magnitude parameter space. Throughout the observing programme, over 300 A-type MS or BHB stars were also observed, the majority of which were previously unknown. For the hot subdwarf stars, we estimate an overall completeness of 90%, with composite hot subdwarfs assumed to be the main contributors to the deficit. By segmenting the sample along the Galactic  $z$ -axis, we model the non-composite hot subdwarf population, finding the best fit with a hyperbolic secant function. The simultaneous fit parameters, mid-plane density ( $\rho_0$ ) and the scale height ( $h_z$ ), are determined as  $5.17 \pm 0.33 \times 10^{-7}$  stars/pc<sup>3</sup> and  $281 \pm 62$  pc, respectively. When accounting for our completeness estimate and the inclusion of composites, assuming a homogeneous distribution,  $\rho_0$  increases to  $\rho_0 = 6.15^{+1.16}_{-0.53} \times 10^{-7}$  stars/pc<sup>3</sup>. While this number is lower than theoretical estimates, it is representative of the local disk population in the solar neighbourhood. Limitations of the fitting procedure include low-number statistics and non-homogeneous Galactic structure across our sample, leading to increased uncertainties, particularly in the scale height. Despite these challenges, our sample is statistically consistent with a homogeneously distributed sample in 3D space when accounting for the scale height, suggesting it as the dominant factor contributing to the varying density across the sample. Our volume-limited sample reveals novel number distributions among hot subdwarf subclasses, including a higher fraction of sdOBs compared to sdBs, a distinction not previously unambiguously identified. However, the true fraction of composite-colour hot subdwarfs remains challenging and is an ambition for future studies. Additionally, we find the commonly adopted selection criterion of  $AEN < 1$  and  $RUWE < 1.4$  is sub-optimal for our sample, especially for the composite hot subdwarf binary population. As an alternative, we propose empirical thresholds to assess the as-

metric solution quality for stars within 500 pc from the *Gaia* database.

Interest in spectroscopically complete, volume-limited samples can only increase in the future. With *Gaia* continuing to offer integral advancements in its unprecedented astrometric solution with every installment, as well as upcoming large-scale spectroscopic surveys like WEAVE (Jin et al. 2023) and 4MOST (de Jong et al. 2019), we can continue to expand our samples at an ever increasing rate. The need for an up-to-date public database, which we continue to work on,<sup>13</sup> is essential, especially if we wish to better organise our knowledge as a community, promote new studies, and drive progress towards ever greater insights onto the nature of hot subluminoous stars in our Galaxy.

**Acknowledgements.** We would like to thank all those involved in the spectroscopic follow-up campaign that has ensued over the recent years. H. D. is and N. R. was supported by the Deutsche Forschungsgemeinschaft (DFG) through grant GE2506/17-1. NR is supported by the DFG through grant RE 3915/2-1. V. S. and M. P. received funding by the Deutsche Forschungsgemeinschaft (DFG) through grants GE2506/9-1 and GE2506/12-1. D.S. acknowledges funding by DFG grant HE1356/70-1. I. P. acknowledges funding from a Warwick Astrophysics prize post-doctoral fellowship, made possible thanks to a generous philanthropic donation, and from a Royal Society University Research Fellowship (URF/R1/231496). JV acknowledges support from the Grant Agency of the Czech Republic (GAČR 22-34467S). The Astronomical Institute Ondřejov is supported by the project RVO:67985815. M. U. gratefully acknowledges funding from the Research Foundation Flanders (FWO) by means of a junior postdoctoral fellowship (grant agreement No. 1247624N). T. S. acknowledges funding from grant SONATA BIS no 2018/30/E/ST9/00398 from the Polish National Science Centre (PI T. Kamiński). RR acknowledges support from Grant RYC2021-030837-I funded by MCIN/AEI/ 10.13039/501100011003 and by “European Union NextGeneration EU/PRTR”. This work was partially supported by the AGAUR/Generalitat de Catalunya grant SGR-386/2021 and by the Spanish MINECO grant PID2020-117252GB-I00. This work has made use of the BeSS database, operated at LESIA, Observatoire de Meudon, France: <http://basebb.obspm.fr>. Some data in this worked came from Guaranteed Observation Time (GTO) based on observations collected at the Centro Astronomico Hispano en Andalucia (CAHA) at Calar Alto, operated jointly by Junta de Andalucia and Consejo Superior de Investigaciones Cientificas (IAA-CSIC). The research has made use of TOPCAT, an interactive graphical viewer and editor for tabular data Taylor (Taylor 2005). This research made use of the SIMBAD database, operated at CDS, Strasbourg, France; the VizieR catalogue access tool, CDS, Strasbourg, France. This work has made use of data from the European Space Agency (ESA) mission *Gaia* (<https://www.cosmos.esa.int/gaia>), processed by the *Gaia* Data Processing and Analysis Consortium (DPAC, <https://www.cosmos.esa.int/web/gaia/dpac/consortium>). Funding for the DPAC has been provided by national institutions, in particular the institutions participating in the *Gaia* Multilateral Agreement. T.K. acknowledges support from the National Science Foundation through grant AST #2107982, from NASA through grant 80NSSC22K0338 and from STScI through grant HST-GO-16659.002-A. Co-funded by the European Union (ERC, CompactBINARIES, 101078773). Views and opinions expressed are however those of the author(s) only and do not necessarily reflect those of the European Union or the European Research Council. Neither the European Union nor the granting authority can be held responsible for them. We thank the survey teams responsible for the copious amount of photometric data available in the literature which we utilised in this work (Henden et al. 2016; DENIS Consortium 2005; Onken et al. 2019; McMahon et al. 2013; Schlafly et al. 2019; Riello et al. 2021; Kato et al. 2007; Høg et al. 2000; van Leeuwen 2007; Girard et al. 2011; Mermilliod 2006; Rufener 1999; Hauck & Mermilliod 1998; Ducati 2002; Spitzer Science 2009; Lucas et al. 2008; Lawrence et al. 2007a,b; Cutri et al. 2021; Bianchi et al. 2017; Yershov 2014; Chambers et al. 2016; Shanks et al. 2015; Page et al. 2012; Abbott et al. 2018; Thompson et al. 1978; Morel & Magnenat 1978; Kilkenny et al. 1988; Lamontagne et al. 2000; Zaritsky et al. 2004; Landolt 2007; Greiss et al. 2012; Norris et al. 1999; Chen et al. 2020; Werner et al. 2021; Bowyer et al. 1995; Kilkenny et al. 1997; O’Donoghue et al. 2013; Kilkenny et al. 2016, 2015; Stetson et al. 2019; Flewelling 2018; Nidever et al. 2021; von Martens et al. 2024; Alam et al. 2015; Monguió et al. 2020; Drlica-Wagner et al. 2022; Abbott et al. 2021; Dixon & Kruk 2009; Gaia Collaboration 2022; Schlafly et al. 2018; Mendes de Oliveira et al. 2019; Edge et al. 2013; Cioni et al. 2011; Minniti et al. 2010; Wamsteker et al. 2000; Meixner et al. 2006).

## References

- Abbott, T. M. C., Abdalla, F. B., Allam, S., et al. 2018, *ApJS*, 239, 18  
 Abbott, T. M. C., Adamów, M., Aguena, M., et al. 2021, *ApJS*, 255, 20  
 Abril, J., Schmidtbreick, L., Ederoclite, A., & López-Sanjuan, C. 2020, *MNRAS*, 492, L40  
 Alam, S., Albareti, F. D., Allende Prieto, C., et al. 2015, *ApJS*, 219, 12  
 Bailer-Jones, C. A. L. 2015, *PASP*, 127, 994  
 Bailer-Jones, C. A. L., Rybizki, J., Fouesneau, M., Demleitner, M., & Andrae, R. 2021, *The Astronomical Journal*, 161, 147  
 Bailer-Jones, C. A. L., Rybizki, J., Fouesneau, M., Mantelet, G., & Andrae, R. 2018, *AJ*, 156, 58  
 Barlow, B. N., Liss, S. E., Wade, R. A., & Green, E. M. 2013, *ApJ*, 771, 23  
 Barlow, B. N., Wade, R. A., Liss, S. E., Østensen, R. H., & Van Winckel, H. 2012, *ApJ*, 758, 58  
 Belokurov, V., Penoyre, Z., Oh, S., et al. 2020, *MNRAS*, 496, 1922  
 Bennett, M. & Bovy, J. 2019, *MNRAS*, 482, 1417  
 Bianchi, L., Shiao, B., & Thilker, D. 2017, *ApJS*, 230, 24  
 Bilir, S., Karaali, S., Ak, S., Yaz, E., & Hamzaoglu, E. 2006, *New A*, 12, 234  
 Binney, J. & Tremaine, S. 1987, *Galactic dynamics* (Princeton University Press)  
 Bodensteiner, J., Shenar, T., & Sana, H. 2020, *A&A*, 641, A42  
 Bovy, J. 2017, *MNRAS*, 470, 1360  
 Bovy, J., Rix, H.-W., Liu, C., et al. 2012, *ApJ*, 753, 148  
 Bovy, J., Rix, H.-W., Schlafly, E. F., et al. 2016, *ApJ*, 823, 30  
 Bowyer, S., Sasseen, T. P., Wu, X., & Lampton, M. 1995, *ApJS*, 96, 461  
 Canbay, R., Bilir, S., Özdönmez, A., & Ak, T. 2023, *AJ*, 165, 163  
 Capitanio, L., Lallement, R., Vergely, J. L., Elyajouri, M., & Monreal-Ibero, A. 2017, *A&A*, 606, A65  
 Castellani, M. & Castellani, V. 1993, *ApJ*, 407, 649  
 Chambers, K. C., Magnier, E. A., Metcalfe, N., et al. 2016, *arXiv e-prints*, arXiv:1612.05560  
 Chen, X., Han, Z., Deca, J., & Podsiadlowski, P. 2013, *MNRAS*, 434, 186  
 Chen, X., Wang, S., Deng, L., et al. 2020, *ApJS*, 249, 18  
 Chornay, N. & Walton, N. A. 2021, *A&A*, 656, A110  
 Cioni, M. R. L., Clementini, G., Girardi, L., et al. 2011, *A&A*, 527, A116  
 Clausen, D. & Wade, R. A. 2011, *ApJ*, 733, L42  
 Clausen, D., Wade, R. A., Kopparapu, R. K., & O’Shaughnessy, R. 2012, *ApJ*, 746, 186  
 Copperwheat, C. M., Morales-Rueda, L., Marsh, T. R., Maxted, P. F. L., & Heber, U. 2011, *MNRAS*, 415, 1381  
 Cox, A. N. 2000, *Allen’s astrophysical quantities*  
 Culpan, R., Geier, S., Reindl, N., et al. 2022, *A&A*, 662, A40  
 Culpan, R., Pelisoli, I., & Geier, S. 2021, *VizieR Online Data Catalog*, J/A+A/654/A107  
 Cutri, R. M., Skrutskie, M. F., van Dyk, S., et al. 2003, *VizieR Online Data Catalog*, II/246  
 Cutri, R. M., Wright, E. L., Conrow, T., et al. 2021, *VizieR Online Data Catalog*, II/328  
 de Jong, R. S., Agertz, O., Berbel, A. A., et al. 2019, *The Messenger*, 175, 3  
 Deca, J., Vos, J., Németh, P., et al. 2018, *MNRAS*, 474, 433  
 DENIS Consortium. 2005, *VizieR Online Data Catalog: The DENIS database*  
 Dixon, W. V. & Kruk, J. W. 2009, in *American Institute of Physics Conference Series*, Vol. 1135, *Future Directions in Ultraviolet Spectroscopy: A Conference Inspired by the Accomplishments of the Far Ultraviolet Spectroscopic Explorer Mission*, ed. M. E. van Steenberg, G. Sonneborn, H. W. Moos, & W. P. Blair, 218–220  
 Dorman, B. & Rood, R. T. 1993, *ApJ*, 409, 387  
 Dorsch, M., Latour, M., Heber, U., et al. 2020, *A&A*, 643, A22  
 Downes, R. A. 1986, *ApJS*, 61, 569  
 Drlica-Wagner, A., Ferguson, P. S., Adamów, M., et al. 2022, *ApJS*, 261, 38  
 Ducati, J. R. 2002, *VizieR Online Data Catalog*  
 Edge, A., Sutherland, W., Kuijken, K., et al. 2013, *The Messenger*, 154, 32  
 El-Badry, K., Conroy, C., Quataert, E., et al. 2022, *MNRAS*, 516, 3602  
 El-Badry, K., Rix, H.-W., & Heintz, T. M. 2021, *MNRAS*, 506, 2269  
 Fairlamb, J. R., Oudmaijer, R. D., Mendigutía, I., Ilee, J. D., & van den Ancker, M. E. 2015, *MNRAS*, 453, 976  
 Feibelman, W. A. 1997, *PASP*, 109, 659  
 Ferguson, D., Gardner, S., & Yanny, B. 2017, *The Astrophysical Journal*, 843, 141  
 Fitzpatrick, E. L., Massa, D., Gordon, K. D., Bohlin, R., & Clayton, G. C. 2019, *ApJ*, 886, 108  
 Flewelling, H. 2018, in *American Astronomical Society Meeting Abstracts*, Vol. 231, *American Astronomical Society Meeting Abstracts #231*, 436.01  
 Fontaine, G., Brassard, P., Charpinet, S., et al. 2012, *A&A*, 539, A12  
 Gaia Collaboration. 2020, *VizieR Online Data Catalog*, I/350  
 Gaia Collaboration. 2022, *VizieR Online Data Catalog*, I/355  
 Gaia Collaboration, Brown, A. G. A., Vallenari, A., et al. 2018a, *A&A*, 616, A1  
 Gaia Collaboration, Brown, A. G. A., Vallenari, A., et al. 2018b, *A&A*, 616, A1  
 Gaia Collaboration, Smart, R. L., Sarro, L. M., et al. 2021, *A&A*, 649, A6  
 Geier, Østensen, R. H., Németh, P., et al. 2017, *A&A*, 600, A50

<sup>13</sup> <https://a15.astro.physik.uni-potsdam.de/w/the-hot-subdwarf/systems/stars/>

- Geier, S. 2020, *A&A*, 635, A193
- Geier, S., Dorsch, M., Pelisoli, I., et al. 2022, *A&A*, 661, A113
- Geier, S., Kupfer, T., Heber, U., et al. 2015, *A&A*, 577, A26
- Geier, S., Raddi, R., Gentile Fusillo, N. P., & Marsh, T. R. 2019, *A&A*, 621, A38
- Gianninas, A., Bergeron, P., Dupuis, J., & Ruiz, M. T. 2010, *ApJ*, 720, 581
- Gianninas, A., Bergeron, P., & Ruiz, M. T. 2011, *ApJ*, 743, 138
- Gilmore, G. & Reid, N. 1983, *MNRAS*, 202, 1025
- Girard, T. M., van Altena, W. F., Zacharias, N., et al. 2011, *AJ*, 142, 15
- Girven, J., Steeghs, D., Heber, U., et al. 2012, *MNRAS*, 425, 1013
- Golovin, A., Reffert, S., Just, A., et al. 2023, *A&A*, 670, A19
- Götberg, Y., de Mink, S. E., Groh, J. H., et al. 2018, *A&A*, 615, A78
- Green, E. M., Fontaine, G., Hyde, E. A., For, B. Q., & Chayer, P. 2008, in *Astronomical Society of the Pacific Conference Series*, Vol. 392, *Hot Subdwarf Stars and Related Objects*, ed. U. Heber, C. S. Jeffery, & R. Napiwotzki, 75
- Green, R. F., Schmidt, M., & Liebert, J. 1986, *ApJS*, 61, 305
- Greenstein, J. L. & Minkowski, R. 1964, *ApJ*, 140, 1601
- Greenstein, J. L. & Sargent, A. I. 1974, *ApJS*, 28, 157
- Greiss, S., Steeghs, D., Gänsicke, B. T., et al. 2012, *AJ*, 144, 24
- Hagen, H. J., Grootte, D., Engels, D., & Reimers, D. 1995, *A&AS*, 111, 195
- Han, Z., Podsiadlowski, P., Maxted, P. F. L., & Marsh, T. R. 2003, *MNRAS*, 341, 669
- Han, Z., Podsiadlowski, P., Maxted, P. F. L., Marsh, T. R., & Ivanova, N. 2002, *MNRAS*, 336, 449
- Hauck, B. & Mermilliod, M. 1998, *A&AS*, 129, 431
- Heber, U. 1986, *A&A*, 155, 33
- Heber, U. 2016, *PASP*, 128, 082001
- Heber, U., Edelmann, H., Lisker, T., & Napiwotzki, R. 2003, *A&A*, 411, L477
- Heber, U., Hunger, K., Jonas, G., & Kudritzki, R. P. 1984, *A&A*, 130, 119
- Heber, U., Irrgang, A., & Schaffenroth, J. 2018, *Open Astronomy*, 27, 35
- Henden, A. A., Templeton, M., Terrell, D., et al. 2016, *VizieR Online Data Catalog*, II/336
- Høg, E., Fabricius, C., Makarov, V. V., et al. 2000, *A&A*, 355, L27
- Hu, H., Dupret, M. A., Aerts, C., et al. 2008, *A&A*, 490, 243
- Humason, M. L. & Zwicky, F. 1947, *ApJ*, 105, 85
- Husser, T. O., Wende-von Berg, S., Dreizler, S., et al. 2013, *A&A*, 553, A6
- Inight, K., Gänsicke, B. T., Breedt, E., et al. 2021, *MNRAS*, 504, 2420
- Irrgang, A., Kreuzer, S., Heber, U., & Brown, W. 2018, *A&A*, 615, L5
- Jin, S., Trager, S. C., Dalton, G. B., et al. 2023, *MNRAS*[arXiv:2212.03981]
- Jurić, M., Ivezić, Ž., Brooks, A., et al. 2008, *ApJ*, 673, 864
- Justham, S., Podsiadlowski, P., & Han, Z. 2011, *MNRAS*, 410, 984
- Kato, D., Nagashima, C., Nagayama, T., et al. 2007, *PASJ*, 59, 615
- Kawka, A., Vennes, S., O'Toole, S., et al. 2015, *MNRAS*, 450, 3514
- Kepler, S. O., Pelisoli, I., Koester, D., et al. 2015, *MNRAS*, 446, 4078
- Kepler, S. O., Pelisoli, I., Koester, D., et al. 2016, *MNRAS*, 455, 3413
- Kepler, S. O., Pelisoli, I., Koester, D., et al. 2019, *MNRAS*, 486, 2169
- Khalack, V., Yameogo, B., LeBlanc, F., et al. 2014, *MNRAS*, 445, 4086
- Kilic, M., Bergeron, P., Kosakowski, A., et al. 2020, *ApJ*, 898, 84
- Kilkenny, D., Heber, U., & Drilling, J. S. 1988, *South African Astronomical Observatory Circular*, 12, 1
- Kilkenny, D., O'Donoghue, D., Koen, C., Stobie, R. S., & Chen, A. 1997, *MNRAS*, 287, 867
- Kilkenny, D., O'Donoghue, D., Worters, H. L., et al. 2015, *MNRAS*, 453, 1879
- Kilkenny, D., Worters, H. L., O'Donoghue, D., et al. 2016, *MNRAS*, 459, 4343
- Kosakowski, A., Brown, W. R., Kilic, M., et al. 2023, *ApJ*, 950, 141
- Kroupa, P. 1992, in *Astronomical Society of the Pacific Conference Series*, Vol. 32, *IAU Colloq. 135: Complementary Approaches to Double and Multiple Star Research*, ed. H. A. McAlister & W. I. Hartkopf, 228
- Kupfer, T., Geier, S., Heber, U., et al. 2015, *A&A*, 576, A44
- Kurucz, R. L. 1996, in *Astronomical Society of the Pacific Conference Series*, Vol. 108, *M.A.S.S., Model Atmospheres and Spectrum Synthesis*, ed. S. J. Adelman, F. Kupka, & W. W. Weiss, 160
- Lallement, R., Vergely, J. L., Valette, B., et al. 2014, *A&A*, 561, A91
- Lamontagne, R., Demers, S., Wesemael, F., Fontaine, G., & Irwin, M. J. 2000, *AJ*, 119, 241
- Landolt, A. U. 2007, *AJ*, 133, 2502
- Lawrence, A., Warren, S. J., Almaini, O., et al. 2007a, *MNRAS*, 379, 1599
- Lawrence, A., Warren, S. J., Almaini, O., et al. 2007b, *MNRAS*, 379, 1599
- Lindgren, L., Hernández, J., Bombrun, A., et al. 2018, *A&A*, 616, A2
- Lindgren, L., Klioner, S. A., Hernández, J., et al. 2021, *A&A*, 649, A2
- Lindgren, L., Lammers, U., Hobbs, D., et al. 2012, *A&A*, 538, A78
- Lucas, P. W., Hoare, M. G., Longmore, A., et al. 2008, *MNRAS*, 391, 136
- Luo, A. L., Zhao, Y. H., Zhao, G., & et al. 2022, *VizieR Online Data Catalog*, V/156
- Ma, X., Hopkins, P. F., Wetzel, A. R., et al. 2017, *MNRAS*, 467, 2430
- Maxted, P. F. L., Heber, U., Marsh, T. R., & North, R. C. 2001, *MNRAS*, 326, 1391
- McMahon, R. G., Banerji, M., Gonzalez, E., et al. 2013, *The Messenger*, 154, 35
- Meixner, M., Gordon, K. D., Indebetouw, R., et al. 2006, *AJ*, 132, 2268
- Mendes de Oliveira, C., Ribeiro, T., Schoenell, W., et al. 2019, *MNRAS*, 489, 241
- Mendez, R. H. & Niemelä, V. S. 1977, *MNRAS*, 178, 409
- Mermilliod, J. C. 2006, *VizieR Online Data Catalog*, II/168
- Mickaelian, A. M. 2008, *AJ*, 136, 946
- Mickaelian, A. M., Nesci, R., Rossi, C., et al. 2007, *A&A*, 464, 1177
- Miller Bertolami, M. M., Althaus, L. G., Unglaub, K., & Weiss, A. 2008, *A&A*, 491, 253
- Minniti, D., Lucas, P. W., Emerson, J. P., et al. 2010, *New A*, 15, 433
- Moehler, S., Heber, U., & de Boer, K. S. 1990a, *A&A*, 239, 265
- Moehler, S., Richter, T., de Boer, K. S., Dettmar, R. J., & Heber, U. 1990b, *A&AS*, 86, 53
- Molina, F., Vos, J., Németh, P., et al. 2022, *A&A*, 658, A122
- Monguió, M., Greimel, R., Drew, J. E., et al. 2020, *A&A*, 638, A18
- Morales-Rueda, L., Maxted, P. F. L., Marsh, T. R., North, R. C., & Heber, U. 2003, *MNRAS*, 338, 752
- Morel, M. & Magnenat, P. 1978, *A&AS*, 34, 477
- Napiwotzki, R., Karl, C. A., Lisker, T., et al. 2004, *Ap&SS*, 291, 321
- Németh, P., Vos, J., Molina, F., & Bastian, A. 2021, *A&A*, 653, A3
- Newell, B. & Sadler, E. M. 1978, *ApJ*, 221, 825
- Nidever, D. L., Dey, A., Olsen, K., et al. 2021, in *American Astronomical Society Meeting Abstracts*, Vol. 53, *American Astronomical Society Meeting Abstracts*, 235.01
- Norris, J. E., Ryan, S. G., & Beers, T. C. 1999, *ApJS*, 123, 639
- O'Donoghue, D., Kilkenny, D., Koen, C., et al. 2013, *MNRAS*, 431, 240
- Onken, C. A., Wolf, C., Bessell, M. S., et al. 2019, *PASA*, 36, e033
- Østensen, R. H. 2004, *Ap&SS*, 291, 263
- Østensen, R. H. 2006, *Baltic Astronomy*, 15, 85
- Otani, T., Lynas-Gray, A. E., Kilkenny, D., et al. 2022, *ApJ*, 926, 17
- Otani, T., Oswalt, T. D., Lynas-Gray, A. E., et al. 2018, *ApJ*, 859, 145
- Paczynski, B. 1971, *Acta Astron.*, 21, 1
- Paczynski, B. 1976, in *Structure and Evolution of Close Binary Systems*, ed. P. Eggleton, S. Mitton, & J. Whelan, Vol. 73, 75
- Page, M. J., Brindle, C., Talavera, A., et al. 2012, *MNRAS*, 426, 903
- Pala, A. F., Gänsicke, B. T., Breedt, E., et al. 2020, *MNRAS*, 494, 3799
- Parker, Q. A., Bojicic, I., & Frew, D. J. 2016, *arXiv e-prints*, arXiv:1603.07042
- Pelisoli, I., Kepler, S. O., Koester, D., & Romero, A. D. 2017, in *Astronomical Society of the Pacific Conference Series*, Vol. 509, *20th European White Dwarf Workshop*, ed. P. E. Tremblay, B. Gänsicke, & T. Marsh, 447
- Pelisoli, I., Vos, J., Geier, S., Schaffenroth, V., & Baran, A. S. 2020, *A&A*, 642, A180
- Penoyre, Z., Belokurov, V., & Evans, N. W. 2022, *MNRAS*, 513, 2437
- Pereira, C. 2011, PhD thesis, Queens University Belfast, Ireland
- Peters, G. J., Wang, L., Gies, D. R., & Grundstrom, E. D. 2016, *The Astrophysical Journal*, 828, 47
- Politano, M., Taam, R. E., van der Sluys, M., & Willems, B. 2008, *ApJ*, 687, L99
- Polis, O. R., Cote, J., Waters, L. B. F. M., & Heise, J. 1991, *A&A*, 241, 419
- Porter, J. M. & Rivinius, T. 2003, *PASP*, 115, 1153
- Prada Moroni, P. G. & Straniero, O. 2009, in *Journal of Physics Conference Series*, Vol. 172, *Journal of Physics Conference Series*, 012011
- Reindl, N., Islami, R., Werner, K., et al. 2023, *arXiv e-prints*, arXiv:2307.03721
- Riello, M., De Angeli, F., Evans, D. W., et al. 2021, *A&A*, 649, A3
- Rufener, F. 1999, *VizieR Online Data Catalog*, II/169
- Saffer, R. A. 1991, PhD thesis, University of Arizona
- Saffer, R. A. & Liebert, J. 1995, in *White Dwarfs*, ed. D. Koester & K. Werner, Vol. 443 (Springer-Verlag), 221
- Sanders, J. L. & Das, P. 2018, *MNRAS*, 481, 4093
- Schaefer, B. E. 2022, *MNRAS*, 517, 6150
- Schaffenroth, J. 2016, Master's thesis, Universität Erlangen-Nürnberg
- Schaffenroth, V., Barlow, B. N., Geier, S., et al. 2019, *A&A*, 630, A80
- Schaffenroth, V., Barlow, B. N., Pelisoli, I., Geier, S., & Kupfer, T. 2023, *A&A*, 673, A90
- Schaffenroth, V., Pelisoli, I., Barlow, B. N., Geier, S., & Kupfer, T. 2022, *A&A*, 666, A182
- Schlafly, E. F., Green, G. M., Lang, D., et al. 2018, *ApJS*, 234, 39
- Schlafly, E. F., Meisner, A. M., & Green, G. M. 2019, *ApJS*, 240, 30
- Science Software Branch at STScI. 2012, *PyRAF: Python alternative for IRAF*, *Astrophysics Source Code Library*, record ascl:1207.011
- Shanks, T., Metcalfe, N., Chehade, B., et al. 2015, *MNRAS*, 451, 4238
- Slettebak, A. & Brundage, R. K. 1971, *AJ*, 76, 338
- Solano, E., Ulla, A., Pérez-Fernández, E., et al. 2022, *MNRAS*, 514, 4239
- Spitzer, Lyman, J. 1942, *ApJ*, 95, 329
- Spitzer Science, C. 2009, *VizieR Online Data Catalog*, II/293
- Stark, M. A. & Wade, R. A. 2003, *AJ*, 126, 1455
- Stetson, P. B., Pancino, E., Zocchi, A., Sanna, N., & Monelli, M. 2019, *MNRAS*, 485, 3042
- Stobie, R. S., Kilkenny, D., O'Donoghue, D., et al. 1997, *MNRAS*, 287, 848
- Sweigart, A. V. 1997, *ApJ*, 474, L23
- Taylor, M. B. 2005, in *Astronomical Society of the Pacific Conference Series*, Vol. 347, *Astronomical Data Analysis Software and Systems XIV*, ed. P. Shopbell, M. Britton, & R. Ebert, 29
- Theissen, A., Moehler, S., Heber, U., & de Boer, K. S. 1993, *A&A*, 273, 524

- Thejll, P., Ulla, A., & MacDonald, J. 1995, *A&A*, 303, 773
- Thompson, G. I., Nandy, K., Jamar, C., et al. 1978, Catalogue of stellar ultraviolet fluxes : a compilation of absolute stellar fluxes measured by the Sky Survey Telescope (S2/68) aboard the ESRO satellite TD-1 /
- Tody, D. 1986, in *Society of Photo-Optical Instrumentation Engineers (SPIE) Conference Series*, Vol. 627, *Instrumentation in astronomy VI*, ed. D. L. Crawford, 733
- Ulla, A. & Thejll, P. 1998, *A&AS*, 132, 1
- van der Kruit, P. C. & Searle, L. 1981a, *A&A*, 95, 105
- van der Kruit, P. C. & Searle, L. 1981b, *A&A*, 95, 116
- van Leeuwen, F. 2007, *A&A*, 474, 653
- Vennes, S., Kawka, A., & Németh, P. 2011, *MNRAS*, 410, 2095
- Villeneuve, B., Wesemael, F., & Fontaine, G. 1995a, *ApJ*, 450, 851
- Villeneuve, B., Wesemael, F., Fontaine, G., Carignan, C., & Green, R. F. 1995b, *ApJ*, 446, 646
- von Martens, R., Marra, V., Quartin, M., et al. 2024, *MNRAS*, 527, 3347
- Vos, J., Németh, P., Vučković, M., Østensen, R., & Parsons, S. 2018, *MNRAS*, 473, 693
- Vos, J., Østensen, R. H., Degroote, P., et al. 2012, *A&A*, 548, A6
- Vos, J., Østensen, R. H., Németh, P., et al. 2013, *A&A*, 559, A54
- Vos, J., Østensen, R. H., Vuckovic, M., & Van Winckel, H. 2017, *A&A*, 605, A109
- Vos, J., Vuckovic, M., Chen, X., et al. 2019, *MNRAS*, 482, 4592
- Wamsteker, W., Skillen, I., Ponz, J. D., et al. 2000, *Ap&SS*, 273, 155
- Wang, L., Gies, D. R., Peters, G. J., et al. 2021, *AJ*, 161, 248
- Webbink, R. F. 1984, *ApJ*, 277, 355
- Wenger, M., Ochsenbein, F., Egret, D., et al. 2000, *A&AS*, 143, 9
- Werner, K. & Rauch, T. 2015, *A&A*, 583, A131
- Werner, M. W., Gorjian, V., Morales, F. Y., et al. 2021, *ApJS*, 254, 11
- Widrow, L. M., Gardner, S., Yanny, B., Dodelson, S., & Chen, H.-Y. 2012, *ApJ*, 750, L41
- Wisotzki, L., Koehler, T., Groote, D., & Reimers, D. 1996, *A&AS*, 115, 227
- Xiang, M., Shi, J., Liu, X., et al. 2018, *ApJS*, 237, 33
- Yanny, B. & Gardner, S. 2013, *ApJ*, 777, 91
- Yershov, V. N. 2014, *Ap&SS*, 354, 97
- Yoachim, P. & Dalcanton, J. J. 2006, *AJ*, 131, 226
- Zaritsky, D., Harris, J., Thompson, I. B., & Grebel, E. K. 2004, *AJ*, 128, 1606
- Zombeck, M., V. 1990, *Handbook of Astronomy and Astrophysics* (Cambridge University Press)
- <sup>17</sup> Instituto de Física, Universidade Federal do Rio Grande do Sul, 91501-900 Porto-Alegre, RS, Brazil
- <sup>18</sup> Nordic Optical Telescope, Rambla José Ana Fernández Pérez, 7, ES-38711 Breña Baja, Spain
- <sup>19</sup> Institute of Astronomy, KU Leuven, Celestijnenlaan 200D, B-3001 Leuven, Belgium
- <sup>20</sup> Isaac Newton Group of Telescopes, Apartado de Correos 368, E-38700 Santa Cruz de La Palma, Spain
- <sup>21</sup> Department of Physics and Astronomy, Aarhus University, Munkegade 120, DK-8000 Aarhus C, Denmark
- <sup>22</sup> Department of Physics and Astronomy, University of Sheffield, Sheffield S3 7RH, UK
- <sup>23</sup> Nicolaus Copernicus Astronomical Centre, ul. Radańska 8, 87-100 Toruń, Poland
- <sup>24</sup> Anton Pannekoek Institute for Astronomy, University of Amsterdam, 1090 GE Amsterdam, The Netherlands
- <sup>25</sup> Hamburger Sternwarte, University of Hamburg, Gojenbergsweg 112, D-21029 Hamburg, Germany

<sup>1</sup> Institute for Physics and Astronomy, University of Potsdam, Karl-Liebknecht-Str. 24/25, 14476 Potsdam, Germany  
e-mail: hdawson@astro.physik.uni-potsdam.de

<sup>2</sup> Dr. Remeis-Sternwarte and ECAP, Astronomical Institute, University of Erlangen-Nürnberg, Sternwartstr. 7, D-96049 Bamberg, Germany

<sup>3</sup> Department of Physics, University of Warwick, Gibbet Hill Road, Coventry CV4 7AL, UK

<sup>4</sup> Thüringer Landessternwarte Tautenburg, Sternwarte 5, D-07778 Tautenburg, Germany

<sup>5</sup> Zentrum für Astronomie der Universität Heidelberg, Landessternwarte, Königstuhl 12, 69117, Heidelberg, Germany

<sup>6</sup> Instituto de Física y Astronomía, Universidad de Valparaíso, Gran Bretaña 1111, Playa Ancha, Valparaíso 2360102, Chile

<sup>7</sup> European Southern Observatory, Alonso de Cordova 3107, Santiago, Chile

<sup>8</sup> Astronomical Institute of the Czech Academy of Sciences, CZ-251 65, Ondřejov, Czech Republic

<sup>9</sup> Department of Astrophysics/IMAPP, Radboud University, P O Box 9010, NL-6500 GL Nijmegen, The Netherlands

<sup>10</sup> Max Planck Institut für Astrophysik, Karl-Schwarzschild-Straße 1, 85748 Garching bei München, Germany

<sup>11</sup> Recogito AS, Storgaten 72, N-8200 Fauske, Norway

<sup>12</sup> Nordic Optical Telescope, Rambla José Ana Fernández Pérez 7, ES-38711 Breña Baja, Spain

<sup>13</sup> Universitat Politècnica de Catalunya, Departament de Física, c/ Esteve Terrades 5, 08860 Castelldefels, Spain

<sup>14</sup> Steward Observatory, University of Arizona, 933 North Cherry Avenue, Tucson, AZ 85721, USA

<sup>15</sup> Leibniz-Institut für Astrophysik Potsdam (AIP), An der Sternwarte 16, 14482 Potsdam, Germany

<sup>16</sup> Armagh Observatory and Planetarium, College Hill, Armagh BT61 9DG, United Kingdom

## **Appendix A: Additional tables**

Table A.1: 500 pc sample of non-composite hot subdwarf stars from *Gaia* DR3, sorted by increasing distance.

Name	RAJ2000	DECJ2000	Class	G	BP-RP	Stilism E(B - V)	E(44-55)	Parallax	Parallax error	RUWE	Reference
HD188112	298.6311	-28.3390	sdB+WD	10.17	-0.32	0.00	0.00	14.002	0.059	1.04	2003A&A...41L..477H
HD149382	248.5972	-4.0145	sdOB	8.89	-0.44	0.00	0.03	13.272	0.064	1.20	1994ApJ...432...351S
BD+284211	327.7957	28.8637	sdO	10.45	-0.54	0.02	0.00	8.917	0.081	1.18	2015A&A...579A...39L
BD+254655	329.9247	26.4324	He-sdO	9.65	-0.47	0.03	0.01	8.679	0.062	1.22	1966VA.....8...63G
HD171858	279.4860	-23.1932	sdB+WD	9.80	-0.35	0.13	0.05	7.245	0.050	0.79	2010A&A...519A...25G
BD+252534	189.3480	25.0665	sdOB	10.46	-0.46	0.01	0.02	7.063	0.066	1.28	2006A&A...452...579O
BD+75325	122.7063	74.9661	He-sdO	9.49	-0.53	0.01	0.00	6.879	0.063	1.30	1997ApJ...485..843L
HD191351	303.3812	-65.0352	sdB	11.31	-0.35	0.01	0.00	5.920	0.051	1.24	2013MNRAS 431..240O
PG0342+026	56.3940	2.7978	sdB	10.93	-0.23	0.09	0.12	5.860	0.052	1.09	2013A&A...557A..122G
HD4539	11.8718	9.9822	sdB	10.26	-0.38	0.01	0.02	5.828	0.079	1.47	2012MNRAS 427.2180N
BD-073477	191.0844	-8.6714	sdB+dM	10.59	-0.36	0.02	0.02	5.800	0.066	1.14	2015A&A...576A..44K
HD127493	218.0894	-22.6572	He-sdO	9.96	-0.43	0.04	0.05	5.721	0.064	1.03	2009PhDT.....273H
CD-321567	60.2723	-32.3961	sdB	11.15	-0.40	0.00	0.02	5.465	0.039	1.14	2013A&A...557A..122G
BD+393226	266.6331	39.3192	He-sdO	10.13	-0.48	0.02	0.02	5.295	0.047	1.12	1981PhDT.....113G
[CW83]0512-08	78.6829	-8.8019	sdOB	11.18	-0.45	0.01	0.04	5.278	0.063	1.36	2013A&A...557A..122G
TYC4406-285-1	215.3652	71.4058	sdB	11.22	-0.39	0.01	0.00	5.239	0.038	0.90	2015MNRAS 450.3514K
[CW83]1758+36	270.0784	36.4823	sdOB	11.30	-0.43	0.02	0.04	5.201	0.045	1.07	2013A&A...557A..122G
EC21494-7018	328.4220	-70.0756	sdB	11.58	-0.37	0.01	0.01	4.886	0.040	1.17	2012MNRAS 427.2180N
HD296955	144.5039	-45.5410	sdB	10.92	-0.35	0.02	0.00	4.879	0.037	1.04	TW
TYC4101-97-1	100.5581	63.6663	sdOB	11.43	-0.41	0.03	0.04	4.831	0.062	1.70	TW
GALEXJ080510.9-105834	121.2951	-10.9766	sdB+WD	12.23	-0.28	0.05	0.05	4.780	0.053	0.96	2012MNRAS 427.2180N
CPD-311701	114.1257	-32.2120	He-sdO	10.47	-0.49	0.01	0.02	4.741	0.052	1.27	2009PhDT.....273H
PG1032+406	158.8186	40.3538	sdB+WD	11.45	-0.46	0.10	0.01	4.730	0.062	1.29	2021ApJS...256...28L
CPD-691434	163.5406	-70.2318	sdOB	11.48	-0.26	0.10	0.14	4.704	0.037	1.06	TW
TYC4427-1021-1	256.2430	73.0785	sdB	10.73	-0.41	0.02	0.00	4.683	0.040	1.23	TW
TYC9044-1653-1	240.0493	-64.5588	He-sdB	11.96	-0.40	0.06	0.05	4.508	0.051	1.07	2012MNRAS 427.2180N
CPD-64481	86.9971	-64.3843	sdB+dM	11.27	-0.42	0.01	0.01	4.431	0.041	1.18	2015A&A...576A..44K
BD+48433	21.7668	49.7096	sdB	11.06	-0.32	0.08	0.08	4.431	0.061	1.21	TW
CD-2315853	298.9093	-23.2285	sdO	11.68	-0.36	0.08	0.12	4.416	0.057	1.21	1983ApJ...270L..13D
Feigs34	159.9032	43.1024	sdO+dM	11.11	-0.49	0.01	0.02	4.410	0.116	2.24	2018A&A...609A..89L
CD-24731	25.9527	-24.0864	sdB+WD	11.68	-0.49	0.01	0.01	4.392	0.069	1.38	2006A&A...452...579O
BD+481777	142.6955	48.2729	He-sdOB	10.64	-0.49	0.01	0.02	4.256	0.069	1.21	2021ApJS...256...28L
HD319179	273.8647	-31.7587	sdB	11.30	-0.20	0.10	0.16	4.244	0.047	0.55	TW
GALEXJ104148.9-073031	160.4534	-7.5087	sdB	11.63	-0.38	0.02	0.03	4.196	0.073	1.44	2012MNRAS 427.2180N
TYC6017-419-1	132.9954	-17.2113	sdOB	11.78	-0.41	0.05	0.06	4.183	0.062	1.28	2012MNRAS 427.2180N
CD-3515910	356.0916	-34.4501	sdB	10.91	-0.43	0.01	0.01	4.169	0.072	1.61	2012MNRAS 427.2180N
BD+423250	286.9189	42.3060	sdB	10.59	-0.33	0.02	0.06	4.151	0.036	1.20	2010A&A...513A...6O
HD205805	324.7947	-46.0977	sdB	10.14	-0.38	0.01	0.01	4.136	0.059	1.14	2006BaltA..15..107P
CD-55317	20.0538	-55.2978	sdOB	11.94	-0.47	0.01	0.00	4.060	0.046	1.01	2016MNRAS 459.4343K
TYC4000-216-1	353.7175	53.7841	sdOB	11.84	-0.40	0.04	0.03	4.035	0.046	1.07	2015MNRAS 450.3514K
TYC4544-2658-1	145.9731	78.5281	sdB	11.11	-0.42	0.01	0.01	3.946	0.044	1.06	2010A&A...513A...6O
HD110942	191.4957	-43.0894	sdB	10.50	-0.19	0.04	0.11	3.942	0.052	1.28	TW
FBS2347+385	357.4485	38.7449	sdB+WD	11.72	-0.19	0.06	0.11	3.939	0.040	0.94	2012MNRAS 427.2180N
TYC1773-399-1	34.4258	28.0582	sdOB	11.76	-0.38	0.08	0.07	3.870	0.062	1.20	2021ApJS...256...28L
CIMelotte20488	50.4155	47.4552	sdB+dM	11.56	-0.11	0.10	0.20	3.865	0.039	1.12	2012MNRAS 427.2180N
TYC5737-1693-1	297.0902	-14.1343	sdB	11.62	-0.16	0.13	0.17	3.805	0.044	0.98	TW
[CW83]0825+15	127.1368	14.8673	He-sdOB	11.62	-0.48	0.02	0.02	3.773	0.064	1.18	2012MNRAS 427.2180N
UCAC4 354-057819	153.4143	-19.3655	sdB	12.57	-0.36	0.02	0.06	3.769	0.068	0.95	TW
TYC4470-864-1	324.5732	72.1856	sdB	11.33	-0.29	0.05	0.05	3.765	0.038	1.12	2021A&A...650A..205V
Feigl10	349.9933	-5.1656	sdOB	11.77	-0.49	0.03	0.02	3.760	0.062	1.14	2014A&A...566A...3R
UCAC4 642-091572	304.6748	38.3053	sdO	11.73	-0.50	0.04	0.03	3.749	0.046	1.11	TW

Continued on next page

Name	RAJ2000	DECJ2000	Class	G	BP-RP	Stilism E(B - V)	E(44-55)	Parallax	Parallax error	RUWE	Reference
TYC467-3836-1	287.5225	2.2844	sdB	11.69	-0.06	0.14	0.22	3.737	0.030	0.85	1986SAAOC.10...27K
PG0909+276	138.2153	27.3421	sdOB	12.18	-0.44	0.02	0.04	3.624	0.079	0.70	2013A&A...557A.122G
TYC8147-498-1	120.7103	-52.2919	sdB	11.87	-0.42	0.04	0.03	3.609	0.045	1.03	TW
TYC7709-376-1	155.8410	-37.6167	sdB+dM	11.69	-0.35	0.04	0.03	3.598	0.046	1.35	2013A&A...553A..18K
PG1352-023	208.7694	-2.5061	sdOB	12.04	-0.47	0.02	0.03	3.594	0.073	1.07	2021ApJS..256...28L
GD1068	30.0552	-17.4790	sdB+dM	12.02	-0.36	0.03	0.04	3.563	0.071	1.13	2016MNRAS.459.4343K
HD345431	300.1797	23.2672	sdOB	11.96	-0.46	0.03	0.02	3.545	0.059	1.05	2021ApJS..256...28L
ATO J029.0051+40.0561	29.0052	40.0559	sdB	11.43	-0.35	0.04	0.06	3.500	0.082	1.26	2023ApJ...942...109L
BD+482721	278.5384	48.4614	sdB	10.66	-0.30	0.02	0.06	3.480	0.033	1.17	2013A&A...557A.122G
LSIV-132	270.5775	-13.1749	sdB	11.70	-0.02	0.27	0.32	3.476	0.042	0.92	TW
CD-229142	177.6619	-23.3430	sdO	11.75	-0.50	0.02	0.00	3.461	0.062	1.09	2010Ap&SS.329..133R
EC14248-2647	216.9475	-27.0193	sdOB	11.96	-0.39	0.05	0.03	3.442	0.066	1.21	2012MNRAS.427.2180N
TYC5917-726-1	85.7715	-16.4827	sdB	12.48	-0.36	0.02	0.05	3.436	0.044	0.74	TW
TYC8827-750-1	343.6857	-55.2518	sdB	12.14	-0.45	0.01	0.01	3.431	0.050	0.98	2012MNRAS.427.2180N
AG+81266	140.3296	81.7241	sdO	11.86	-0.54	0.02	0.01	3.397	0.054	1.08	2018A&A...609A..89L
CD-3914181	319.0115	-38.4991	sdB	10.95	-0.32	0.01	0.00	3.328	0.060	1.14	2015MNRAS.453.1879K
UCAC4 604-016003	74.5074	30.6000	sdB	13.00	0.03	0.22	0.29	3.306	0.030	1.00	TW
UCAC4157-007263	95.0479	-58.6514	sdO	11.84	-0.50	0.02	0.01	3.254	0.051	1.21	TW
TYC9399-770-1	135.1694	-77.6159	sdB	12.31	-0.21	0.14	0.13	3.242	0.036	1.14	TW
HD76431	86.1897	30.6481	sdB	12.41	-0.44	0.03	0.13	3.224	0.053	0.93	2021ApJS..256...28L
TYC999-248-1	261.1893	11.5404	sdB	12.57	-0.29	0.10	0.09	3.215	0.061	1.02	2021ApJS..256...28L
CD-399849	231.5294	-39.4888	sdB	12.07	-0.39	0.06	0.04	3.212	0.079	1.20	2017A&A...600A..50G
HD350426	295.8800	18.4094	sdO	12.02	-0.48	0.04	0.03	3.200	0.088	1.12	TW
PG0133+114	24.1092	11.6588	sdB+Wd	12.28	-0.34	0.04	0.07	3.196	0.099	0.83	2018A&A...609A..89L
EC02200-2338	35.5828	-23.4156	sdB+Wd	11.99	-0.40	0.02	0.01	3.162	0.061	1.07	2016MNRAS.459.4343K
PG0057+155	14.9863	15.7372	sdOB	12.04	-0.43	0.06	0.04	3.152	0.062	1.03	2005A&A...430.223L
CPD-201123	91.5558	-20.3521	He-sdB+Wd	12.04	-0.33	0.01	0.05	3.128	0.055	1.34	2020MNRAS.497...67L
PG1233+427/Feige65	188.9631	42.3776	sdB	11.97	-0.41	0.02	0.01	3.087	0.054	1.17	2021ApJS..256...28L
LSII+2221	301.2396	22.3444	sdO	12.49	-0.56	0.03	0.02	3.084	0.065	0.68	1981MNRAS.197..241W
GALEXJ063952.0+515658	99.9672	51.9502	sdB	11.94	-0.38	0.04	0.05	3.084	0.055	1.05	2012MNRAS.427.2180N
HZ1	72.5563	17.7018	He-sdO	12.57	-0.08	0.28	0.26	3.073	0.042	0.74	2007A&A...462...269S
[CW83]1419-09	215.6680	-9.2896	sdO+Wd	12.02	-0.46	0.03	0.04	2.992	0.073	1.16	2022A&A...661A.113G
Feige 11	16.0904	4.2268	sdB+Wd	12.03	-0.39	0.05	0.02	2.989	0.057	0.86	2008A&A...477L..13G
PG1452+198	223.6659	19.6168	sdB+Wd	12.43	-0.39	0.03	0.05	2.986	0.060	0.70	2021ApJS..256...28L
BD+182647	190.4658	17.5220	sdO	11.75	-0.53	0.03	0.02	2.983	0.087	1.37	2018A&A...609A..89L
UCAC4282-094834	250.8441	-33.7016	sdB	13.09	-0.02	0.26	0.27	2.977	0.029	0.98	TW
LAMOSTJ092239.81+270225.2	140.6661	27.0403	sdOB+Wd	12.59	-0.47	0.02	0.01	2.973	0.087	0.70	2021ApJS..256...28L
UCAC4 575-030949	99.1572	24.8570	sdB	12.84	-0.31	0.02	0.00	2.951	0.060	0.96	TW
EC15103-1557	228.2930	-16.1392	sdB	12.81	-0.29	0.08	0.05	2.941	0.049	0.83	2017OAS...26..164G
GSC00141-01628	96.5928	4.0733	sdB	12.31	-0.37	0.02	0.03	2.928	0.056	0.92	2021ApJS..256...28L
TYC4563-2614-1	231.7208	79.6919	sdOB	11.64	-0.49	0.03	0.01	2.927	0.049	1.31	TW
TYC4824-1079-1	110.3765	-4.1699	sdB	12.41	-0.39	0.03	0.02	2.920	0.065	0.76	TW
5842817473052628480	185.2214	-71.4384	sdB	13.05	0.16	0.29	0.37	2.907	0.020	1.04	TW
2MASSJ19110167+8716038	287.7579	87.2677	sdB	12.71	-0.35	0.07	0.07	2.885	0.042	0.78	2012MNRAS.427.2180N
UCAC4 278-224220	302.4073	-34.5254	sdOB	12.48	-0.38	0.06	0.07	2.877	0.052	1.02	TW
TYC4407-187-1	192.7039	74.6621	sdB	11.55	-0.41	0.02	0.01	2.876	0.042	1.13	TW
TYC5977-517-1	109.9191	-21.8895	sdB+dM/BD	12.13	-0.36	0.03	0.01	2.869	0.056	0.91	2023A&A...673A.90S
CD-3011223	212.8173	-30.8844	sdB+Wd	12.30	-0.39	0.04	0.03	2.865	0.066	0.90	2013A&A...554A..54G
HD269696/AA Dor	82.9180	-69.8837	sdOB+rM/BD	11.10	-0.48	0.03	0.03	2.864	0.049	0.84	2011A&A...531L...7K
LSI+63198	52.2739	64.0783	sdOB	12.71	-0.15	0.12	0.06	2.856	0.032	0.81	2022SchneiderPhDT
SBSS1709+535	257.5551	53.4461	sdB	12.59	-0.38	0.02	0.01	2.852	0.045	0.82	2021ApJS..256...28L
UCAC4 686-011641	29.5873	47.0618	sdB	12.37	-0.31	0.09	0.03	2.806	0.067	0.99	TW
CD-403927	122.6323	-40.5466	sdO	12.18	-0.51	0.02	0.01	2.801	0.056	0.94	1988SAAOC..12....1K

Continued on next page



Name	RAJ2000	DECJ2000	Class	G	BP-RP	Stilism E(B - V)	E(44-55)	Parallax	Parallax error	RUWE	Reference
LSIV+0021	307.8263	1.0904	sdOB	12.39	-0.44	0.05	0.04	2.784	0.067	0.62	1991A&A...250..370B
PG1519+640	230.1309	63.8691	sdB+dM/WD	12.38	-0.42	0.02	0.02	2.759	0.050	0.80	2013A&A...557A.122G
[CW83]0711+22	108.6244	22.2831	He-sdO	11.59	-0.49	0.02	0.02	2.751	0.049	0.97	2021Aps...256...28L
UCAC4 350-080079	243.6771	-20.0086	sdB	12.97	-0.01	0.28	0.31	2.736	0.038	0.84	TW
HZ44	200.8966	36.1332	He-sdOB	11.61	-0.50	0.02	0.02	2.735	0.063	1.33	2021Aps...256...28L
TYC9516-559-1	197.9130	-88.0869	sdOB	12.12	-0.25	0.09	0.15	2.688	0.038	1.02	TW
FBS0102+362	16.2035	36.4618	sdOB	12.38	-0.43	0.03	0.03	2.684	0.067	0.72	2021Aps...256...28L
PG0011+283	3.5927	28.6154	sdB	12.63	-0.35	0.05	0.03	2.661	0.060	0.68	2021Aps...256...28L
[CW83]0832-01	128.8495	-1.9313	He-sdO	11.37	-0.48	0.02	0.02	2.653	0.075	1.19	2009PhDT.....273H
UCAC4169-132984	235.3229	-56.2659	sdOB	13.30	-0.16	0.18	0.19	2.648	0.028	0.88	TW
HD269665	82.7416	-68.7529	sdOB	11.13	-0.46	0.03	0.03	2.647	0.061	1.12	1989AJ....97..88IH
UCAC4 228-097826	235.3455	-44.4066	sdOB	13.12	-0.33	0.08	0.10	2.637	0.043	1.00	TW
LAMOSTJ213129.05+195157.0	322.8711	19.8658	sdO	13.14	-0.43	0.05	0.05	2.636	0.045	0.93	2021Aps...256...28L
CD-33417	17.1116	-32.7199	sdB	12.21	-0.40	0.01	0.00	2.634	0.070	1.04	1984A&A...130..119H
TYC3281-978-1	31.2653	46.2643	sdB	11.50	-0.26	0.08	0.11	2.630	0.046	1.09	2021Aps...256...28L
TYC7489-686-1	331.4668	-31.6844	sdB+dM/BD	12.33	-0.35	0.01	0.04	2.620	0.056	0.74	2012MNRAS.427.2180N
TYC6343-1675-1	311.4515	-21.6006	sdOB	12.58	-0.44	0.03	0.04	2.621	0.063	0.65	TW
Ballon90100001	348.8396	29.0837	sdBV	12.08	-0.32	0.05	0.08	2.620	0.046	0.86	2008ASPC...392..301O
UCAC4 436-075435	272.0031	-2.9518	sdOB	13.95	0.45	0.19	0.60	2.619	0.020	1.06	TW
UCAC4 314-235772	290.9293	-27.2806	sdB	13.16	-0.36	0.09	0.09	2.604	0.060	1.02	TW
UCAC4 219-125136	250.4592	-46.3492	sdB	13.10	-0.10	0.18	0.19	2.594	0.034	1.00	TW
CPD-5510148	0.8891	-54.7170	sdB	11.93	-0.41	0.01	0.00	2.582	0.048	1.12	TW
LSIV-0617	280.4612	-6.4166	sdB	11.58	-0.24	0.17	0.16	2.571	0.048	0.91	TW
TYC3133-2416-1	288.8154	43.6742	sdB	12.44	-0.39	0.02	0.02	2.566	0.047	0.73	2021Aps...256...28L
Feige108	349.0517	-1.8432	sdB+W/D	12.98	-0.39	0.04	0.07	2.555	0.076	1.01	1994Apl...432..351S
[J92b]MarkA	310.9969	-10.7949	sdO	13.22	-0.41	0.04	0.06	2.553	0.045	0.93	2017A&A...600A..50G
TYC770-941-1	108.0100	11.5590	sdB	12.44	-0.39	0.01	0.02	2.540	0.071	0.77	2021Aps...256...28L
UCAC4 280-113383	256.9890	-34.1135	sdOB	13.09	0.04	0.26	0.31	2.533	0.024	0.80	TW
TYC2701-1209-1	315.8853	30.5938	sdOB	12.92	-0.36	0.04	0.08	2.529	0.040	0.81	2021Aps...256...28L
NGC 1360/CPD-26 389	53.3110	-25.8715	O(H)	11.25	-0.56	0.01	0.00	2.520	0.073	1.64	1977MNRAS.178..409M
CPD-56464	42.5900	-56.2146	sdB	11.94	-0.43	0.01	0.00	2.502	0.043	1.08	1991A&A...242..175V
PG0215+183	34.5658	18.5272	sdB	13.42	-0.17	0.08	0.15	2.491	0.063	1.18	1986Aps...61..305G
TYC3556-3568-1	294.6359	46.0664	sdB+dM	12.11	-0.34	0.02	0.05	2.476	0.039	0.92	2010MNRAS.408L..51O
TYC8293-1755-1	226.7167	-46.7156	He-sdO	12.12	-0.37	0.05	0.12	2.476	0.076	0.99	TW
LB1766	74.8284	-53.8817	He-sdB	12.28	-0.48	0.01	0.01	2.469	0.045	0.81	2010MNRAS.409..582N
GALEXJ042034.8+012041	65.1453	1.3447	He-sdO	13.27	-0.21	0.16	0.12	2.465	0.032	0.95	2012MNRAS.427.2180N
UCAC4 190-121347	239.4466	-52.0704	sdB	13.27	-0.21	0.02	0.00	2.465	0.032	0.95	TW
PG 1604+504	241.3922	50.3145	sdOB	12.93	-0.44	0.02	0.00	2.458	0.047	0.88	1986Aps...61..305G
UCAC4 335-187276	281.6388	-23.0642	sdB	13.77	0.21	0.25	0.45	2.450	0.028	1.01	TW
PN A66 36/EC 13379-1937	205.1724	-19.8820	O(H)	11.49	-0.47	0.06	0.04	2.450	0.070	1.26	ZieglerPhDT
220023158877454208	337.4641	58.9592	sdB	14.40	-0.01	0.25	0.25	2.449	0.019	0.99	TW
UCAC4 364-079928	256.2398	-17.3841	sdOB	13.97	0.02	0.29	0.34	2.447	0.025	0.90	TW
GD1099	28.2118	-16.5919	sdB	13.48	-0.38	0.04	0.05	2.441	0.056	1.03	1989SAOC..13...69K
CD-3019716	358.1505	-30.1693	sdO+W/D	12.05	-0.51	0.01	0.02	2.427	0.070	0.98	2000AJ....119..241L
RL105	67.8011	42.9861	sdB	14.54	0.04	0.14	0.28	2.424	0.085	2.64	2021Aps...256...28L
KPD0005+5106	2.0759	51.3879	O(He)	13.27	-0.48	0.08	0.05	2.423	0.043	1.04	2015A&A...583A.131W
PG1538+401	235.1627	39.9302	sdB	13.20	-0.46	0.02	0.03	2.423	0.038	1.00	2021Aps...256...28L
V*EQPsc	353.6443	-1.3271	sdB+dM	13.02	-0.33	0.03	0.03	2.419	0.059	0.99	2019MNRAS.489.1556B
UCAC4 332-167523	278.3422	-23.7178	sdB	12.81	0.01	0.25	0.27	2.408	0.037	0.81	TW
TYC8532-976-1	87.1888	-58.2900	sdOB	13.05	-0.39	0.02	0.06	2.400	0.063	1.25	2013A&A...557A.122G
GALEXJ19498-2806	297.4519	-28.1133	sdB	12.99	-0.35	0.10	0.07	2.399	0.052	1.00	2017A&A...600A..50G
LSIV-14116	314.4120	-14.4295	He-sdO	12.95	-0.44	0.03	0.04	2.378	0.069	0.85	2021MNRAS.501..623J
TYC5285-201-1	39.1784	-8.8578	sdB	12.54	-0.40	0.02	0.01	2.372	0.070	0.88	TW
FBS1715+424	259.3283	42.4358	sdO	12.45	-0.53	0.03	0.00	2.369	0.050	0.63	2021Aps...256...28L

Continued on next page

Name	RAJ2000	DECJ2000	Class	G	BP-RP	Stilism E(B - V)	E(44-55)	Parallax	Parallax error	RUWE	Reference
LAMOSTJ121002.71+250358.2	332.5114	25.0661	sdB	12.81	-0.23	0.05	0.07	2.368	0.043	0.87	2021ApJS..256..28L
FBS1133+754	174.1395	75.1149	sdOB	13.15	-0.39	0.03	0.06	2.365	0.036	0.88	2012MNRAS.427.2180N
KUV16256+4034	246.8188	40.4579	sdB+dM/WD	12.54	-0.38	0.02	0.00	2.365	0.044	0.90	2021ApJS..256...28L
[CW83]1735+22	264.3600	22.1494	sdO+WD	11.80	-0.45	0.04	0.04	2.348	0.055	1.34	2010A&A...519A..25G
6849135629120266624	304.3944	-25.1402	sdB	12.89	-0.30	0.09	0.08	2.347	0.055	0.81	TW
TYC497-63-1	305.8858	1.6057	sdB	12.87	-0.32	0.06	0.08	2.347	0.056	0.70	2012MNRAS.427.2180N
PG1610+529	242.8389	52.7682	sdB	12.75	-0.39	0.02	0.06	2.346	0.047	0.91	2021ApJS..256...28L
CD-249052	156.4620	-24.8888	He-sdO	11.70	-0.48	0.03	0.03	2.341	0.063	1.32	2009PhDT.....273H
UCAC4.635-004580	20.9384	36.9631	sdB	13.12	-0.39	0.04	0.04	2.340	0.050	0.97	TW
EC21027-3301	316.4484	-32.8312	sdO	13.44	-0.46	0.07	0.06	2.339	0.054	1.00	2015MNRAS.453.1879K
EC20106-5248	303.6082	-52.6567	sdB	12.54	-0.36	0.03	0.02	2.337	0.177	2.68	2013A&A...557A.122G
Feige14	27.0154	-5.9294	sdB	12.74	-0.38	0.03	0.01	2.327	0.058	0.85	1958ApJ...128..267F
Feige36	324.0057	-72.8076	sdB+dM	12.34	-0.34	0.03	0.05	2.316	0.045	0.77	2010A&A...519A..25G
UCAC4.507-015874	166.1317	24.6619	sdB+dM	12.72	-0.39	0.02	0.03	2.312	0.056	0.95	1999ASPC...169..546E
140.5535	88.2498	11.3128	sdOB	13.32	-0.16	0.24	0.22	2.284	0.032	0.94	TW
TYC7691-3990-1	140.5535	-39.0237	sdB	12.73	-0.36	0.04	0.03	2.283	0.040	0.77	TW
GALEX J191509.0-290311	263.885	-50.2567	sdB	12.92	-0.41	0.01	0.00	2.276	0.041	0.73	1989SAAOC..13...69K
HZ3	288.7882	-29.0527	He-sdO	13.22	-0.29	0.09	0.11	2.275	0.044	1.04	2017A&A...600A..50G
TYC5859-1253-1	58.3806	10.7511	sdB	12.80	-0.27	0.20	0.15	2.264	0.072	0.98	2021ApJS..256...28L
Feige95	32.4138	-18.1739	sdB	13.12	-0.43	0.03	0.01	2.256	0.047	1.02	2022SchneiderPhDT
PG0314+146	49.4084	14.7732	He-sdO	13.21	-0.42	0.02	0.04	2.247	0.057	1.34	2021ApJS..256...28L
PG1232-136	188.8279	-13.9191	sdB+dM/WD	12.50	-0.19	0.18	0.19	2.245	0.065	1.03	2012MNRAS.427.2180N
EVR-CB-001	132.0645	-74.3151	sdB+WD	13.23	-0.37	0.02	0.03	2.245	0.042	0.92	2015A&A...576A..44K
2MASSJ09112370-2415462	137.8488	-24.2629	sdOB	12.57	-0.16	0.10	0.09	2.243	0.039	0.94	2019ApJ...883...51R
TYC4651-1475-1	248.0599	85.2329	sdB	13.57	-0.27	0.07	0.12	2.238	0.032	1.03	TW
LAMOSTJ180933.32+223059.9	272.3890	22.5167	sdOB + WD	12.32	-0.34	0.12	0.09	2.231	0.044	0.85	2012MNRAS.427.2180N
HD265435	103.3512	33.0595	sdOB + WD	12.09	-0.27	0.07	0.10	2.230	0.035	0.84	2021ApJS..256...28L
LSIV+092	263.9314	9.1436	sdB+dM/BD	12.68	-0.20	0.12	0.14	2.214	0.050	0.77	2017A&A...600A..50G
PG2337+070	355.0197	7.2858	sdB	13.45	-0.15	0.08	0.18	2.210	0.038	1.08	2021ApJS..256...28L
2MASSJ02065617+1438585	31.7341	14.6495	sdB	13.34	-0.34	0.07	0.08	2.210	0.054	1.05	2012MNRAS.427.2180N
GALEXJ07015-6717	105.3926	-67.2946	sdOB	13.13	-0.39	0.04	0.05	2.198	0.032	1.07	2017A&A...600A..50G
TYC9249-242-1	193.0616	-72.9138	sdB	12.97	-0.19	0.16	0.14	2.192	0.034	1.00	TW
Ton788	228.6350	24.1780	sdB+WD	13.18	-0.36	0.05	0.06	2.190	0.041	1.10	2021ApJS..256...28L
KUV20417+7604	310.1953	76.2444	sdB	12.73	-0.20	0.17	0.14	2.187	0.036	0.99	1987AJ.....94.1271W
5881540795158796416	224.2913	-55.4395	sdB	14.06	-0.13	0.15	0.21	2.180	0.027	0.99	TW
PG2349+002	357.9717	0.4715	sdB	13.26	-0.34	0.03	0.07	2.176	0.043	1.08	2013A&A...557A.122G
TYC1969-78-1	155.2731	22.9907	sdB	12.66	-0.42	0.02	0.00	2.176	0.069	0.63	TW
UCAC4.095-055105	219.0558	-71.1940	sdB	12.95	-0.21	0.12	0.12	2.171	0.038	1.00	TW
PG1710+490	258.0782	48.9766	sdB	12.83	-0.40	0.03	0.05	2.167	0.041	0.77	2013A&A...557A.122G
TYC4542-482-1	154.5052	75.2244	sdB+dM/BD	12.68	-0.24	0.03	0.10	2.166	0.039	0.83	2022ApJ...928...20B
US719	143.4494	46.0750	sdB	12.37	-0.41	0.02	0.00	2.166	0.062	0.66	2017A&A...600A..50G
PB7352	343.9300	-6.9944	sdB+dM/WD	12.27	-0.35	0.04	0.03	2.153	0.069	0.91	2015A&A...576A..44K
Feige91	212.1341	59.6738	sdB	13.40	-0.45	0.02	0.00	2.143	0.033	0.97	1974ApJS..28..157G
5917224379858067712	257.1978	-56.6804	sdB	14.01	-0.18	0.12	0.12	2.141	0.030	1.04	TW
EC11575-1845	180.0235	-19.0344	sdO+dM	13.09	-0.26	0.04	0.16	2.138	0.067	2.32	2015ApJ...808..179D
PG1207-033	182.4004	-3.5521	sdOB	13.33	-0.45	0.03	0.03	2.134	0.058	0.99	2005A&A...430.223L
CD-48106	7.9237	-47.4223	sdBV	12.36	-0.40	0.01	0.00	2.134	0.049	0.74	1984A&A...130..119H
PG0918+029	140.3674	2.7672	sdB+WD	13.28	-0.45	0.03	0.03	2.133	0.059	1.04	2021ApJS..256...28L
FBS2154+329	329.2756	33.1365	sdOB	13.39	-0.33	0.07	0.07	2.123	0.035	1.01	2008AJ...136..946M
LAMOSTJ064618.36+292013.2	101.5765	29.3370	sdO	13.57	-0.45	0.03	0.04	2.118	0.050	1.04	2021ApJS..256...28L
UCAC4.435-106149	298.7121	-3.1255	He-sdOB	13.22	0.02	0.22	0.36	2.114	0.021	0.95	TW
UCAC4.174-038075	146.4025	-55.2652	sdB	12.82	-0.36	0.04	0.02	2.109	0.046	0.82	TW
UCAC4.198-195239	349.9556	-50.5634	sdOB	13.07	-0.48	0.01	0.00	2.103	0.043	0.94	TW

Continued on next page

Name	RAJ2000	DECJ2000	Class	G	BP-RP	Stilism E(B - V)	E(44-55)	Parallax	Parallax error	RUWE	Reference
FBS2253+335	343.9925	33.7199	sdB	12.75	-0.26	0.07	0.12	2.102	0.050	0.85	2021ApJS..256...28L
Feige38	169.2056	6.9925	sdB	12.98	-0.37	0.03	0.06	2.098	0.071	1.04	2013A&A...557A.122G
TomS183	15.3232	-33.7127	sdB+Wd	12.58	-0.41	0.01	0.01	2.090	0.059	0.76	2010A&A...519A.25G
PG1722+286	261.0498	28.5908	sdOB	13.33	-0.45	0.03	0.04	2.090	0.033	1.02	2021ApJS..256...28L
PG0004+133	1.8907	13.5992	sdB	13.05	-0.13	0.05	0.22	2.090	0.036	0.93	2021ApJS..256...28L
TYC769-1149-1	114.5485	10.6264	sdB	11.80	-0.45	0.02	0.03	2.076	0.071	1.19	TW
TYC1117-348-1	318.6130	13.3685	sdOB	13.69	-0.31	0.05	0.07	2.076	0.066	1.31	TW
PHL1548	52.2809	-11.7056	sdOB	13.26	-0.37	0.03	0.09	2.074	0.038	1.13	2013A&A...557A.122G
UCAC4.178-120735	213.7422	-54.4676	sdOB	13.48	-0.14	0.20	0.21	2.073	0.028	1.06	TW
BPSC522947-0196	290.9424	-47.7881	sdB	13.29	-0.36	0.04	0.09	2.068	0.040	1.01	1992AJ....103..267B
UCAC4.540-131404	305.7445	17.8390	sdOB	13.02	-0.45	0.03	0.03	2.066	0.047	0.87	TW
HE0247-0418	42.5997	-4.1040	sdB	13.00	-0.39	0.03	0.03	2.060	0.060	0.92	2012MNRAS.427.2180N
EC21556-5552	329.7529	-55.6343	sdB+Wd	13.10	-0.39	0.01	0.02	2.049	0.040	1.04	2011MNRAS.415.1381C
PG1634+061	249.2649	5.9848	sdB	13.82	-0.34	0.06	0.08	2.048	0.096	2.78	2021ApJS..256...28L
UCAC4.285-089547	243.7561	-33.1560	sdOB	13.46	-0.23	0.28	0.17	2.047	0.035	1.05	TW
UCAC4.575-018970	86.1719	24.9196	sdB	13.60	-0.21	0.13	0.13	2.036	0.039	1.08	TW
Feige46	174.3595	14.1704	He-sdO	13.24	-0.48	0.02	0.02	2.035	0.060	1.00	2019ApJ...881....7L
GALEXJ18599-6749	349.3620	7.8680	sdB+Wd	13.72	-0.28	0.05	0.09	2.032	0.043	1.20	2013A&A...557A.122G
Feige109	284.9928	-67.8287	sdB	13.22	-0.35	0.04	0.05	2.030	0.034	1.02	2017A&A...600A..50G
LSIV+109	310.7603	10.5725	He-sdO	11.95	-0.44	0.08	0.05	2.030	0.060	1.05	2018A&A...620A..36S
PG1619+522	245.1613	52.1025	sdB+Wd	13.23	-0.45	0.02	0.03	2.027	0.040	1.10	1994ApJ...432..351S
LSII+091	299.6914	10.0190	sdB	12.79	-0.33	0.07	0.04	2.026	0.056	0.81	TW
EC23073-6905	347.6483	-68.8252	sdB	12.54	-0.40	0.02	0.01	2.022	0.048	0.88	2022MöllerMSCT
2MASSJ21352819+4903391	323.8677	49.0609	sdB	13.61	-0.30	0.08	0.03	2.017	0.027	1.11	TW
UCAC4.202-168220	271.7187	-49.6211	sdB	13.13	-0.28	0.09	0.09	2.016	0.045	1.05	TW
PG1544+488	236.5484	48.6438	He-sdOB+He-sdOB	12.77	-0.44	0.02	0.05	2.014	0.046	0.75	2021ApJS..256...28L
GALEXJ10415+1842	160.3767	18.7027	sdOB	12.97	-0.46	0.02	0.02	2.014	0.068	1.10	2021ApJS..256...28L
UCAC4.149-221427	354.7874	-60.2195	sdB	13.31	-0.37	0.01	0.00	2.009	0.033	1.04	TW
LAMOSTJ044847.21-040016.9	72.1968	-4.0049	sdB+dM/BD	13.35	-0.39	0.03	0.05	2.007	0.049	1.18	2021ApJS..256...28L
2MASSJ15292631+7011543	232.3599	70.1983	sdB+Wd	12.44	-0.36	0.02	0.00	2.006	0.048	0.78	2022ApJ...928...20B
GALEXJ19111-1406	287.7885	-14.1149	He-sdO	11.88	-0.27	0.17	0.14	2.005	0.054	1.00	2021MNRAS.501..623J
6028436785642385152	254.9810	-31.2995	sdB	14.01	-0.21	0.16	0.11	2.005	0.035	0.97	TW
UCAC4.299-079624	229.5817	-30.2446	sdB	13.72	0.00	0.20	0.31	2.004	0.024	0.97	TW
TYC 6800-72-1	249.6178	-24.8532	He-sdO	12.11	-0.05	0.29	0.32	2.002	0.034	0.83	TW
UCAC4488-012508	83.2798	7.5061	sdOB	13.79	-0.17	0.18	0.21	1.999	0.032	1.07	2021ApJS..256...28L
MWP 1	319.2845	34.2077	PG1159	13.02	-0.53	0.25	0.03	1.991	0.045	0.95	1993A&A...268..561M
UCAC4.451-072127	267.4836	0.1100	sdOB	14.34	0.09	0.06	0.36	1.984	0.025	1.02	2021ApJS..256...28L
UCAC4.497-042535	110.6667	9.2318	sdO	13.03	-0.52	0.02	0.01	1.984	0.067	0.90	2021ApJS..256...28L
UCAC4.067-027932	260.0518	-76.6077	sdB	13.54	-0.18	0.05	0.16	1.982	0.022	1.04	2017A&A...600A..50G
EC11119-2405	168.5918	-24.3582	sdB	12.76	-0.26	0.03	0.07	1.976	0.053	0.84	2011MNRAS.410.2095V
GD1110	349.8517	-8.8773	sdB	12.92	-0.39	0.05	0.03	1.967	0.075	0.81	2010A&A...513A...60
LSIII+4850	337.4885	48.3578	sdOB	12.23	-0.32	0.02	0.07	1.965	0.041	0.94	TW
UCAC4.349-002972	43.2902	-20.2426	sdO	12.03	-0.49	0.02	0.01	1.955	0.083	0.97	TW
EC12408-1427	190.8751	-14.7303	sdB+Wd	12.78	-0.39	0.02	0.03	1.939	0.065	0.66	1997MNRAS.287..867K

TW (This Work): Spectroscopically identified or reclassified in this work.

Table A.2: 500 pc sample of composite hot subdwarf stars from *Gaia* DR3 ad identified through IR excess in their SED fits (Sec. 5.3), sorted by increasing distance.

Name	RAJ2000	DECJ2000	Class	G	BP-RP	Stilism E(B - V)	Parallax	Parallax error	RUWE	Reference
BD+102357	178.9860	9.8471	sdO+A8V*	8.81	0.16	0.01	5.883	0.035	1.21	1980A&A....85...367B
HD 185510	294.9119	-6.0639	sdB+KOIII*	7.80	1.39	0.11	5.600	0.028	0.97	1992AJ....103..267B
SB290	10.7432	-38.1271	sdB+K7V	10.42	-0.32	0.00	5.485	0.164	3.18	2013A&A...557A.122G
BD+341543	107.5323	34.4147	sdB+F9V*	10.05	0.33	0.01	5.143	0.044	2.05	2013A&A...559A..54V
BD-035357	330.1519	-2.7408	sdOB+G8III*	9.06	1.20	0.07	4.770	0.039	2.05	1982MNRAS...201..901D
CD-243988	96.0465	-24.5307	sdOB+G6V	10.68	0.28	0.01	4.406	0.086	4.93	TW
GD319	192.5183	55.1004	sdB+K3V	12.67	-0.42	0.02	4.039	0.053	0.72	2021ApJS...256...28L
PG1104+243	166.8590	24.0530	sdOB+G0V	11.20	0.22	0.02	3.467	0.070	2.30	2012A&A...548A...6V
CD-441028	48.3133	-43.9164	sdOB+F7V	10.72	0.22	0.01	3.458	0.049	2.08	TW
TYC4454-1229-1	300.9430	71.6068	sdO+G5V	10.40	0.02	0.04	3.452	0.092	3.56	TW
BD+293070	264.5883	29.1466	sdB+F8V*	10.29	0.34	0.02	3.428	0.043	2.43	2013A&A...559A..54V
PG0749+658	118.6019	65.7021	sdB+K1V	12.06	-0.02	0.03	3.370	0.132	4.49	1994ApJ...432..351S
TYC4890-19-1	135.5186	-7.3465	sdOB+M0(TW)	12.02	-0.35	0.02	3.335	0.069	1.20	2017MNRAS...466.5020H
CPD-73420	104.4036	-73.4133	sdB+G	11.74	-0.17	0.09	3.290	0.038	1.18	2012MNRAS...427.2180N
GD274	16.7959	51.1727	sdOB+G5V	12.08	0.37	0.09	3.281	0.105	4.59	2021ApJS...256...28L
TYC7831-110-1	220.5407	-43.2968	sdB+K3V	11.78	-0.30	0.06	3.199	0.144	2.30	TW
BD-11162	13.0626	-10.6629	sdO+G0V	11.08	0.01	0.03	3.063	0.119	3.69	1953PASP...65...48V
CPD-71172	43.3781	-71.3756	sdOB+F2V*	10.61	0.30	0.03	3.059	0.021	0.93	1988A&A...205...147V
TYC5337-1128-1	83.7761	-10.5912	sdB+F6V	11.57	0.23	0.03	2.976	0.055	2.18	TW
GD1053	29.1329	-13.9078	sdOBV+K1V(TW)	12.25	-0.26	0.05	2.866	0.140	2.02	2010A&A...513A...60
TYC 1703-394-1	336.9935	20.1063	sdB+F5V*	10.64	0.39	0.04	2.858	0.032	1.61	2012MNRAS...427.2180N
SDSSJ185859.95	284.7499	17.3032	sdB+F8V*	11.83	0.58	0.13	2.809	0.042	2.11	2017A&A...600A..50G
LSIV+065	285.3290	6.2493	sdOB+K1V	12.35	-0.15	0.23	2.773	0.046	1.11	TW
TYC6906-318-1	305.2490	-22.8341	sdB+G2V	11.68	0.26	0.09	2.710	0.086	3.82	2012MNRAS...427.2180N
UCAC4 235-080231	223.6418	-43.0661	sdB+G9V	12.76	0.08	0.06	2.699	0.094	2.98	TW
CD-488608	209.1215	-49.5676	sdOB+K0V	12.16	-0.06	0.07	2.677	0.061	1.52	2012MNRAS...427.2180N
TYC2084-448-1	264.2134	28.1096	sdB+F6V*	11.45	0.40	0.03	2.605	0.022	1.31	2012MNRAS...427.2180N
TYC7644-1857-1	114.2603	-38.9095	sdO+G2V	12.65	0.19	0.08	2.529	0.054	2.58	TW
EC05053-2806	76.8343	-28.0403	sdB+G0V	12.43	0.09	0.01	2.495	0.043	1.29	2013MNRAS...431..2400
TYC1337-283-1	98.8248	20.5924	He-sdOB+A0V*	11.40	0.25	0.02	2.488	0.414	6.62	2019ApJ...881.....7L
UCAC4 275-013588	104.3408	-35.1936	sdOB+K1V	13.15	0.13	0.08	2.446	0.103	5.55	TW
441779188809043328	233.0570	1.0806	sdOB+K7V	12.77	-0.15	0.05	2.405	0.123	2.31	TW
HDE283048	58.3072	25.7560	He-sdO+FV*	10.12	0.49	0.13	2.386	0.055	2.71	2023ApJ...942..109L
Feige87	205.0614	60.8796	sdB+G0V	11.61	-0.05	0.02	2.302	0.097	3.73	2012MNRAS...427.2180N
TYC499-2297-1	302.4654	3.1755	sdB+K3V(TW)	12.66	-0.20	0.07	2.299	0.141	2.33	2012MNRAS...427.2180N
ClMelotte 22 AK IV-859	60.8945	26.0663	sdB+F7V*	12.27	0.37	0.20	2.291	0.049	2.04	2023ApJ...942..109L
PG2317+046	349.9807	4.8762	sdO+KV	12.79	-0.29	0.05	2.290	0.065	0.93	2013A&A...557A.122G
GD299	144.5848	55.0969	He-sdOB+K3V	12.01	-0.35	0.02	2.265	0.056	1.15	2021ApJS...256...28L
UCAC4 716-006410	11.8897	53.0791	sdB+K6V	12.94	-0.16	0.09	2.241	0.039	0.89	TW
SB744	27.1839	-26.6038	sdOB+G1V	12.22	0.03	0.01	2.221	0.095	2.60	2000AJ....119..241L
NGC 1514/HD 281679	62.3207	30.7760	O(H)+A*	9.28	0.81	0.29	2.203	0.019	1.05	1997PASP..109..659F
TYC3871-835-1	228.9095	56.8955	sdB+G0V*	11.37	0.32	0.02	2.164	0.036	1.95	2014ASPC...481..265V
EC11031-1348	166.4225	-14.0734	sdB+F6*	11.43	0.44	0.03	2.156	0.027	0.98	2012MNRAS...427.2180N
TYC4401-1269-1	216.7852	72.9638	sdB+F3V*	11.14	0.19	0.02	2.105	0.027	1.51	TW
EC20217-5704	306.4240	-56.9140	sdOB+K3V(TW)	12.43	-0.30	0.03	2.030	0.109	1.32	2013MNRAS...431..2400
EC11429-2701	176.3692	-27.3066	sdB+F2V*	11.29	0.39	0.03	2.022	0.033	1.03	1997MNRAS...287..867K
GALEXJ02342+2342	38.5552	23.7030	sdB+F5V*	12.14	0.54	0.10	2.021	0.024	1.22	2017A&A...600A..50G
PHL 1079	24.6125	3.6608	sdB+G7V	13.27	0.11	0.03	1.924	0.108	4.67	2012ApJ...758...58B

TW (This Work): Spectroscopically identified or reclassified in this work. (TW) Previously known hot subdwarf system, but with a newly identified cool MS companion.  
 \* (asterix) Previously known systems manually added to the sample. Companion spectral classes are derived from our SED based effective temperature estimates using the calibration given in Cox (2000).

Table A.3: Other underluminous objects

Name	RAJ2000	DECJ2000	Class	Reference
PB5919	5.8918	6.9465	CV	TW
ATO J005.9853+42.7854	5.9854	42.7855	CV	2023AJ....165..148H
PG0038+199	10.3974	20.1546	DO1	2017A&A...601A...8W
HD9478	22.7583	-66.4967	BV9	1975mcts.book.....H
V*BGTri	26.1982	32.5499	CV	2008PZP.....8....4K
V*BOCet	31.6636	-2.0619	CV	1993PASP..105..127D
BD+14341	31.7211	15.2949	CV	1966PASP...78..279W
300394067131824768	31.8226	30.0865	WD	2022yCat.5156....0L
UCAC4 693-013549	31.9930	48.5754	CV	2017AJ....153..204S
2MASS J02150626+0155041	33.7760	1.9176	sdA	2023ApJ...950..141K
FBS0212+385	33.9933	38.7721	DAO	2021ApJS..256...28L
1RXS J022917.1-395851	37.3208	-39.9838	CV	2018MNRAS.473..693V
HS0229+8016	38.9930	80.4957	CV	2005A&A...443..995A
V*IMEri	66.1715	-20.1200	CV	2001PASP..113..764D
HD30112	71.1753	0.5680	B3/5V	1999MSS...C05....0H
HD31726	74.4362	-14.2320	MSB	TW
V*V1159Ori	82.2481	-3.5646	CV	1992A&A...259..198J
V*UYOriA	83.0013	-4.9316	Herbig Ae	2015MNRAS.453..976F
V*TWPic	83.7107	-58.0280	CV	1984BAAS...16..514S
V*CNOri	88.0324	-5.4168	CV	TW
TYC1325-1524-1	90.4308	21.5494	BHB	TW
HD43112	93.7854	13.8512	B1V	2020A&A...639A..81B
TYC144-2049-1	94.6424	5.8229	MSA/BHB	TW
UCAC4 316-011308	95.9167	-26.9641	CV	2020ATel14219....1S
EGB4	97.3915	71.0766	CV	1983ApJS...53..523W
HD47144B	98.8503	-36.7799	-	-
V*RR Pic	98.9003	-62.6401	CV	1950PASP..62..221H
3378090704289927552	100.6357	20.9336	-	-
TYC6526-2311-1	104.6056	-25.4155	MSA/BHB	TW
ASASJ071404+7004.3	108.5197	70.0716	CV	2022MNRAS.510.3605I
TYC6545-1888-1	110.1178	-27.6298	BHB	TW
3053791570751929344	112.0746	-8.1706	-	-
2MASSJ07465548-0934305	116.7312	-9.5752	CV	2008MNRAS.385.1485P
TYC5999-40-1	121.2186	-17.0072	MSA/BHB	TW
TYC6560-514-1	123.5778	-24.8821	-	-
V*IXVel	123.8288	-49.2228	CV	1984AJ....89..389E
PG0834+501	129.4056	49.8743	DAO.8	2011ApJ...743..138G
586495788772380672	142.3875	7.7051	MSA/BHB	2022yCat.5156....0L
V*ERUMa	146.8000	51.9025	CV	1993PASP..105..127D
TYC834-791-1	147.0800	13.4886	MSA/BHB	TW
V*RWSex	154.9858	-8.6990	CV	1974ApJ...189L.131G
PG1034+001	159.2654	-0.1385	DO	1983BAAS...15Q.984S
BD-112966	162.9262	-12.4026	BHB	TW
5389717630410364160	165.0685	-42.6771	CV	TW
CD-416382	167.6733	-42.2374	BHB	TW
5371969485515378176	174.5655	-48.5888	-	-
HS1136+6646	174.7733	66.5048	DAO+KV	2021A&A...647A.184R
5377677187816453632	177.2208	-46.4381	-	-
6058834949182961536	180.9110	-60.3801	sdA	TW
Feige55	181.1601	60.5354	DAO	2011ApJ...743..138G
V*AMCVn	188.7278	37.6290	AMCVn	1966ApJ...144..496G
TYC7791-1293-1	201.1430	-41.1065	CV	1995PASP..107..846D
V*UXUMa	204.1703	51.9138	CV	1949ApJ...110..387M
BD+302431	204.6031	29.3651	BHB	2018A&A...618A..86S
V*V827 Cen	206.0665	-51.0125	ApSiCr	1978mcts.book.....H
CPD-731185	206.2093	-74.1253	BHB	TW
HD135485	228.9386	-14.6931	B3V	1988mcts.book.....H
V*HPLib	233.9710	-14.2201	AMCVn	1994MNRAS.271..910O

Continued on next page

Table A.3: Other underluminous objects

Name	RAJ2000	DECJ2000	Class	Reference
V*LXSer	234.5003	18.8676	CV	1979IBVS.1630....1S
2MASSJ16360160+5944411	249.0069	59.7447	CV	2022ApJ...928...20B
LSIV-08 1	249.0907	-8.1101	BHB	TW
V*V1084Her	250.9404	34.0443	CV	2001PASP..113..764D
V*V341Ara	254.4225	-63.2111	CV	1995PASP..107..846D
ATO J256.7330-24.9840	256.7331	-24.9841	WD+dM?	TW
2MASSJ17514575+3820157	267.9406	38.3378	DA	2023A&A...677A..29R
TYC4213-1610-1	270.3466	65.9479	MSF	1981ApJS...45..437A
TYC8357-3863-1	272.1239	-45.7673	-	-
CPD-634369	274.7516	-63.3007	CV	1995PASP..107..846D
V*V603Aql	282.2277	0.5841	CV	TW
HD337604	286.4118	25.6505	pre-ELM/sdB candidate	TW
V*MVLyr	286.8179	44.0188	CV	1981ApJ...245..644S
HD231084	289.4615	13.4102	BHB	TW
TYC3556-325-1	292.8714	45.9849	CV	2013ApJ...775...64G
4318061098980872960	294.0047	14.5094	sdA	TW
TYC3135-86-1	294.7834	37.5719	pre-ELM/sdB candidate	TW
HD186605A	295.9462	38.3223	MSB	TW
6684666865906605568	296.2970	-44.9985	DAO	2023A&A...677A..29R
CD-4214462	296.9191	-42.0075	CV	1971PASP..83..485B
V*ABDrac	297.2770	77.7398	CV	1995A&AS..114..269D
M27	299.9016	22.7212	DAO.6	2011ApJ...743..138G
ATO J300.8707+08.6463	300.8707	8.6464	DAO+MS	2023AJ....165..142K
HD194375	303.6092	80.5317	MSB	TW
V*CMDel	306.2372	17.2983	CV	1982A&AS...48..383V
HBHA4204-09	316.9677	44.0950	CV	1997AAHam..11....1K
TYC546-1349-1	323.5281	3.5709	CV	2021ApJS..256...28L
V*LSPeg	327.9915	14.1147	CV	1986ApJ...300..779S
V*UUAqr	332.2740	-3.7717	CV	1986ApJ...300..779S
NGC 7293/PHL 287	337.4108	-20.8372	DAO.5	2011ApJ...743..138G
V*AOPsc	343.8250	-3.1779	CV	1984MNRAS.210..663M
[PS72]97	345.8481	-26.2500	sdA	2023ApJ...950..141K
GD1532	347.5466	-32.7012	WD	TW
V*CGTuc	352.2545	-63.1107	ApSi	1975mcts.book.....H

- Candidates that have been removed from the sample as they either possess poor astrometry or are too bright to be genuine hot subdwarfs (see Sec. 2.2.)

(TW) (This Work): Spectroscopically identified or reclassified in this work.